Arabian Journal of Geosciences (2022) 15: 1172
https://doi.org/10.1007/s12517-022-10412-y

ORIGINAL PAPER

# The Soma polymetallic hydrothermal Pb–Zn-Cu(± Mo ± Ag ± Au) mineralizations in the south of Biga Peninsula, NW Turkey: constraints from mineralogy, geochemistry, and fluid inclusion data

Mustafa Kumral[1] · Mohammed Kabiru[1] · Mustafa Selman Aydogan[2] · Huseyin Kocaturk[1] · Ali Tugcan Unluer[1]

Received: 15 December 2021 / Accepted: 31 May 2022 / Published online: 16 June 2022


**Abstract**
The NW Anatolia of Turkey (especially the Biga Peninsula) hosts substantial skarn, porphyry Cu-Mo, and epithermal Pb–Zn ± Ag ± Au mineralizations. Of these, ore-forming processes of the Soma (Manisa) region in the southern part of the Biga Peninsula are distinguished. Two subtypes of mineralization zones were identified in the study area. The first subtype of mineralization is located nearby outward sections of Turkali pluton, resembling a porphyry type of mineralization with higher homogenization temperatures (197.5 to 280.1 ℃) with salinities 2.4 to 15.8 wt.% NaCl equivalents. The relatively high anomalies of Cu (up to 0.36% and Mo up to 634 ppm) with minor gold anomalies found in outward zones of Turkali pluton suggested the pluton likely to host higher-grade porphyry-type mineralization. The mineralogical assemblage of Turkali-related mineralization consists of chalcopyrite and molybdenite with minor sphalerite and also points out a granite-hosted porphyry-hydrothermal system. The second subtype of mineralization which is located around Yayladalı village can be described as a volcanic-hosted polymetallic Pb–Zn ± Au ± Ag hydrothermal-type mineralization. The main ore minerals are galena and sphalerite with supergene minerals including smithsonite and cerussite; therefore, this mineralization can be considered as a volcanic-hosted multiphase hydrothermal polymetallic deposition. The homogenization temperatures of 191.5 to 251.4 ℃ with salinities 5.86 to 18.0 wt. NaCl equivalents also support this conclusion. Both mineralization fields have high alteration index values, as expected. The volcanic-hosted mineralization zone has higher Ishikawa Alteration Index (AI) and chlorite carbonate pyrite index (CCPI) values, probably caused by the higher permeability of acidic volcanic rocks with lots of fractures.

**Keywords** Polymetallic mineralization · Soma · Biga peninsula · Fluid inclusions · Hydrothermal alteration · Porphyry Cu-Mo deposits

## Introduction

Post-collisional Cenozoic magmatic activities have occurred extensively in northwestern Anatolia following an Eocene continent-arc collision. Especially, the magmatic pulses are characterized in the Biga Peninsula in the northern part of the İzmir-Ankara-Erzincan Neotethyan suture zone (Aldanmaz 2006; Dilek and Atunkaynak 2009, and *references therein*). The Biga Peninsula is a tectonically complex region in northwestern Turkey, and numerous causative granitic bodies and volcanic products are well-exposed (Black et al. 2012) in this region. In the last three decades, there has been a remarkable increase in the exploration targets of mineral deposits related to magmatic products.

The region has an ancient history of both base and precious metal endowments, which were abandoned due to low grades of the time or inferior existing technology to make them economically viable. This metalogenic belt provided a suitable environment from Eocene to Oligo-Miocene magmatism and volcanism-related mineralization of different deposit types. The metallic deposits in the region have been extensively studied and classified as Pb–Zn-Cu skarn and porphyry Cu-Mo ± Au to epithermal Au–Ag deposits (Yigit

Responsible Editor: Murat Karakus

✉ Mustafa Kumral
kumral@itu.edu.tr

[1] Department of Geological Engineering, Faculty of Mines, Istanbul Technical University, TR34467 Istanbul, Turkey

[2] Department of Geological Engineering, Faculty of Engineering, Balıkesir University, TR10145 Balıkesir, Turkey

2006; 2007; 2009; 2012; Özpınar et al. 2012; Akiska et al. 2013; Sánchez et al. 2016; Kuşcu et al. 2019).

Pb–Zn deposits of NW Turkey are hosted by Miocene volcanic as vein or breccia along fault zones and as replacement bodies in skarn zones between granitic suits and carbonate rocks (Hedenquist et al. 2000; Yilmaz et al. 2010; Smith et al. 2014; Leroux 2016; Akiska, 2020). Especially, Pb–Zn-bearing mineral deposits are classified into low, intermediate, and high sulphidation epithermal systems, but most of base metal-rich epithermal deposits in the region fall under intermediate sulphidation epithermal style within volcanic lava surrounded by intense hydrothermal alterations (Pirajno 1995; Yilmaz et al. 2010; Cicek and Oyman 2016).

The recent studies about base metal and precious metal-bearing polymetallic hydrothermal systems evaluate the genetic origin and evolution of hydrothermal mineralizations by using ore paragenesis, alteration mineralogy, fluid inclusion, and isotope studies in Biga Peninsula (Yilmaz et al. 2007; Gökce and Bozkaya 2007; Kasapçı et al. 2008; Bozkaya and Gökce 2009; Yilmaz et al. 2013; Bozkaya and Banks 2016; Cicek and Oyman 2016; Kabiru 2017; Kabiru et al. 2018; Bozkaya et al. 2014, 2016, 2018, 2020; Sari et al. 2021).

Despite the fact that there has been significant research carried out for different kinds of polymetallic hydrothermal systems around the Biga Peninsula, some of the newly discovered possible sources of the Soma region are still subjects to debate because of the lack of systematic evaluation for geochemical analyses and fluid inclusion studies in that region. The previous studies outlined above by the authors mainly indicated the origin and type of the mineral deposits related to the Biga Peninsula; however, it is hard to reach robust information on the spatial relationship and ore-forming processes of the Soma region in the southern part of the Biga Peninsula.

Cu-Mo-Pb–Zn ± Ag ± Au polymetallic mineralizations in the Soma region (Manisa, NW Turkey) have the same characteristics with plenty of similar deposits not only in Biga Peninsula and NW Turkey but also across the globe. Thus, we examine possible ore-forming sources and processes around the Soma region to shed light on additional constraints for time-consuming new research in the region and literature such as rapidly quantifying alteration, possible mineral targets, spatial zonation, and fluid characteristics with the associated magmatic occurrences. The fluid inclusion studies clearly indicate the existence of both porphyry-hydrothermal-type mineralizations within the plutonic rocks and a volcanic-hosted hydrothermal system which was effective on the andesitic rocks.

## Geological setting

The study area is situated in the southern part of the Biga Peninsula in northwestern Turkey, about 33 km from the city of Soma (Fig. 1). The basement rocks of this region are composed mainly of strongly deformed and partly metamorphosed clastics and volcanic series, the so-called Karakaya Complex, representing a subduction-accretion process (Bingöl et al., 1973; Tekeli 1981). The Karakaya Complex of the Permian and Triassic age is subdivided into two tectonostratigraphic units; Nilüfer unit consisting of metabasite, intercalation of phyllite, and marble series which is overlain by Hodul unit comprised of arkosic sandstone, shale, and siltstone intercalations followed by sandstone, siltstone, conglomerate with Permian limestone olistostrome on top, and finally by greywacke, shale, chert, limestone, and spilitic volcanic rock series (Okay et al. 1991; Okay and Göncüoğlu 2004; Sayit and Göncüoglu 2009; Altunkaynak and Yilmaz 1999; Okay and Altiner 2004; Özdamar et al. 2021).

The study area is dominated by basement rocks comprising metapelite and metabasite overlaid uncomfortably by Triassic sedimentary sequence. The lower section of this sequence is composed of fine-grained detrital sediments of marl, shale, and limestone. The upper sequence overlies uncomfortably the lower sequence with medium-coarse-grained, yellow to whitish, well-sorted feldspathic sandstone which grades upward to fine-medium-grained, gray-greenish, siltstone and dark brown greywacke, thick layered-massive, partially recrystallized micritic gray-white Permian limestone (Okay and Göncüoğlu 2004).

A shear matrix characterizes the sediments deposited adjacent to steeply dipping approximately N-S or NE-SW trending faults, representing deposits from a fluvial and lacustrine environment (Altunkaynak and Yilmaz 1999). These basement rocks are covered by unconformably alternating with Neogene volcano-sedimentary (Fig. 1). The clastic sedimentary rocks of Neogene are surrounded or passed into volcanic rocks and consist of the lower and upper sequences. Volcano-sedimentary rocks observed include gray-white thinly bedded tuffs of plagioclase and biotite with limited extent or impregnated with a block of lapilli, volcanogenic clays. The volcanic rocks overlie uncomfortably the metamorphic rock and are composed of high K-calc-alkaline andesite, basaltic-andesite, trachyandesite, and dacite.

Oligocene–Miocene calc-alkaline volcanism with contemporaneous magmatism has a cogenetic association as the magma changes from calc-alkaline to alkaline, which may result from tapping from a zoned magma chamber (Yilmaz 1989; Aldanmaz 2006; Altunkaynak and Genç 2008; Seghedi et al. 2015; Ersoy et al. 2017).

## Analytical methods

Fifty samples were collected from andesites, breccia, and stockwork vein orebodies during geological mapping. After petrographic investigations, the selected samples were

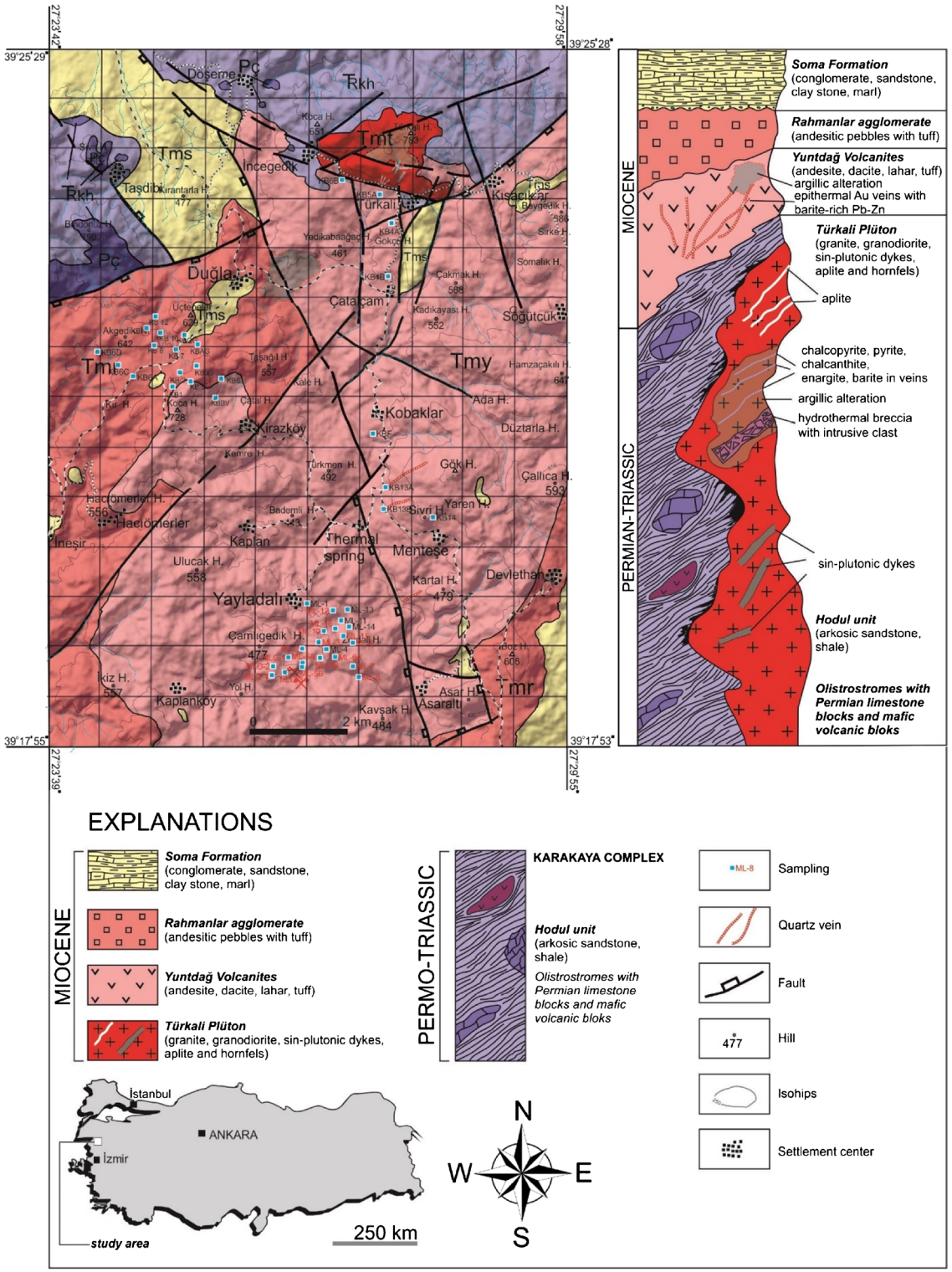


**Fig. 1** Geological map and simplified stratigraphic section of the study area

prepared for geochemistry, ore microscopy, and fluid inclusion studies at the Geochemical Laboratories of Istanbul Technical University. Whole-rock analyses were conducted on thirty samples. The ore and altered samples were crushed by a crusher to 2 mm, dried under a controlled temperature at 105 ℃ for 16 h, and pulverized using a Tungsten Carbide ring mill pulverizer to 40 µm. Pellets were made using a powdered sample, aluminum cup, boric acid, and wax for

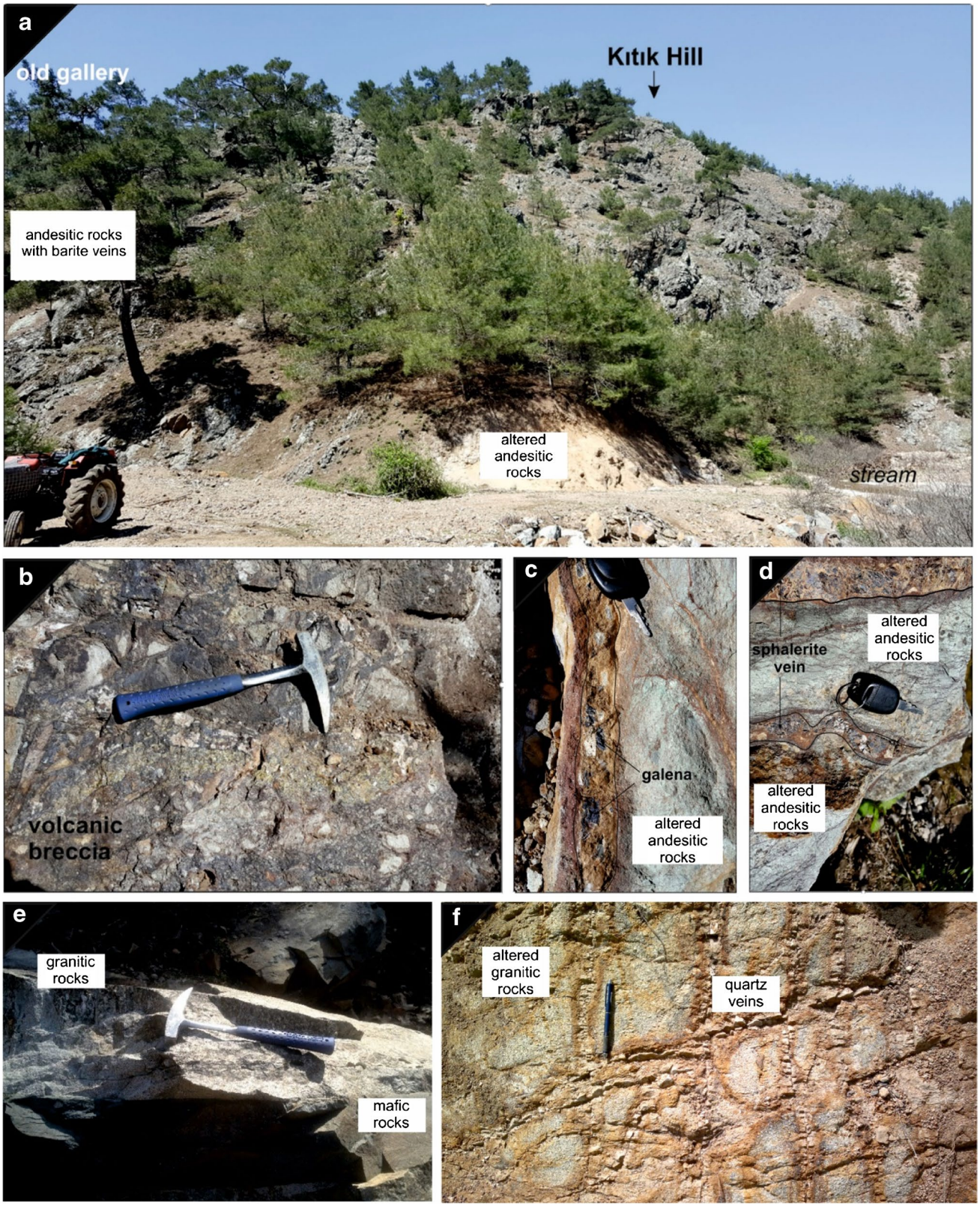


**Fig. 2** Field photographs of Yayladalı mineralizations. (**a**) Position of altered andesite hosting mineralizations, barite veins, and old galery. (**b**) Volcanic breccia. (**c**) Galena vein cutting altered andesite. (**d**) Brown-colored sphalerite vein cutting altered andesite. (**e**) Granitic rocks of Turkali pluton and mafic dike. (**f**) Altered granitic rocks of Turkali pluton with stockwork quartz veins

major element analyses, while the powdered sample and Polysium were used for trace element analysis. The prepared samples were analyzed using BRUNKER S8 TIGER model X-ray fluorescence spectrometer with a wavelength ranging from 0.01 to 12 nm for major and minor elements. Trace, rare earth element (REE), and platinum group of elements (PGEs) were analyzed inductively coupled plasma-mass spectrometry (ICP-MS). A 100 mg of an oven-dried powdered sample was digested in two steps. The first step was completed using 6 ml of 35% HCl and 2 ml of 65% HNO3 (3:1/Aqua-Regia) to dissolve sulfide ores since it is strongly oxidized. A 1 ml of 38–40% HF was added to the Aqua-Regia solution to dissolve silicate minerals, controlled pressure and temperature using a Teflon tube (inert to many acids), with a Berghoff microwave at 135 ℃. The second step

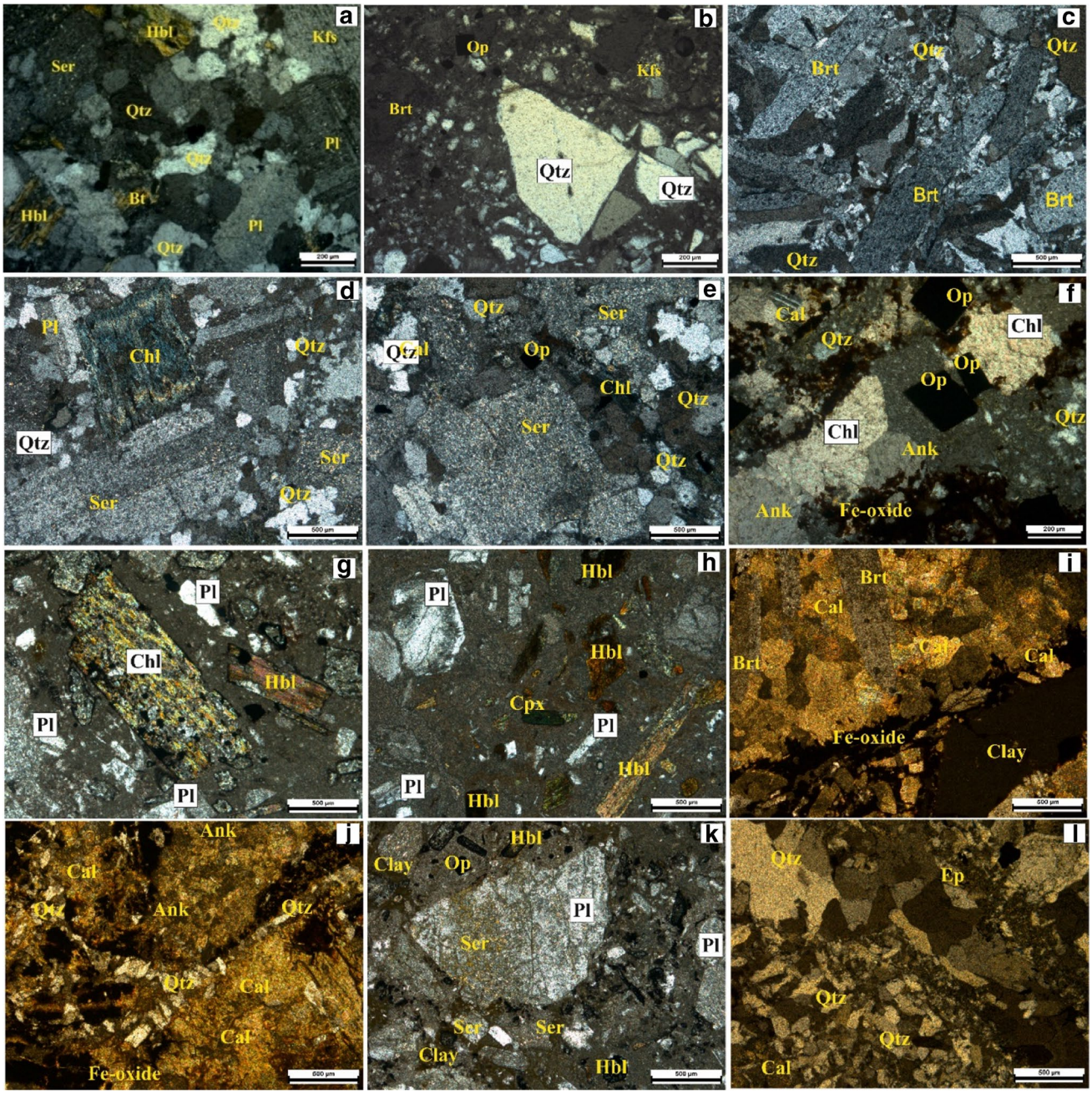


**Fig. 3** Photomicrographs of the mineral assemblages in the Turkali pluton (**a**–**f**) and Yuntdagı volcanites from the Yayladalı mineralization field (**g**–**l**). Abbreviations: plagioclase (pl), chlorite (chl), hornblende (hbl), sericite (ser), barite (brt), calcite (cal), quartz (qtz), anglesite (ang), cerrusite (cer), galena (gn), barite (brt), sphalerite (sp), pyrite (py), orpiment (orp), realgar (rlg), chalcopyrite (cpy), calcite (cal)

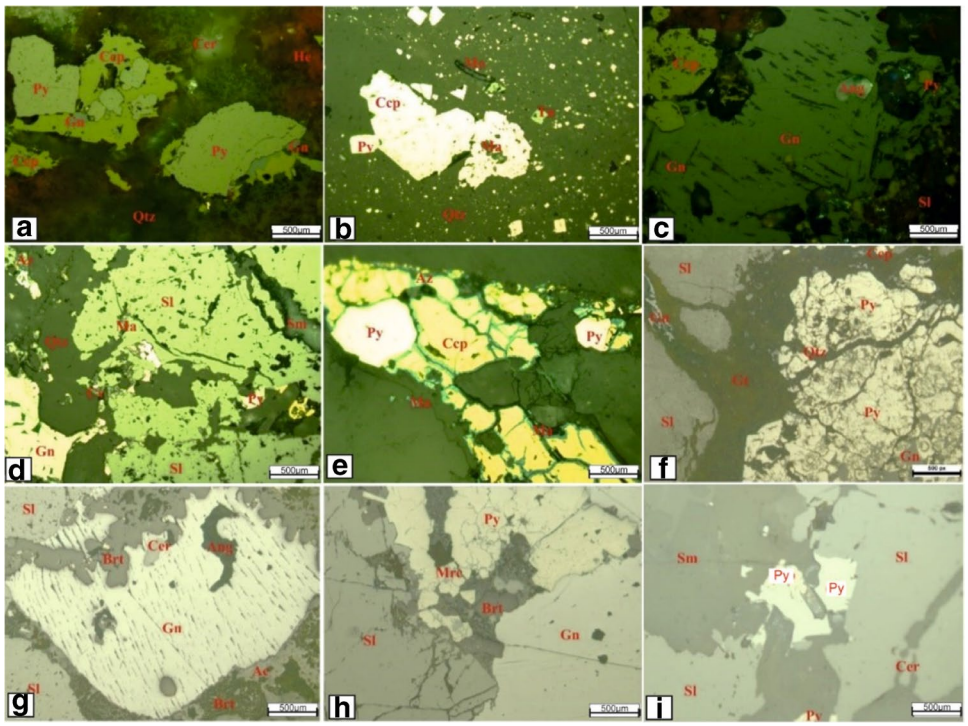


**Fig. 4** Photomicrographs of the ore mineral assemblages in the Turkali pluton (**a**–**e**) and Yuntdagı volcanites from the Yayladalı mineralization field (**g**–**i**). Abbreviations: barite(brt), quartz (Qtz), anglesite (ang), cerrusite (cer), galena (gn), barite (brt), sphalerite (sl), pyrite (py), chalcopyrite (cpy),smithsonite (sm), calcite (cal), molybdenite (mo), tenantite (Tn)

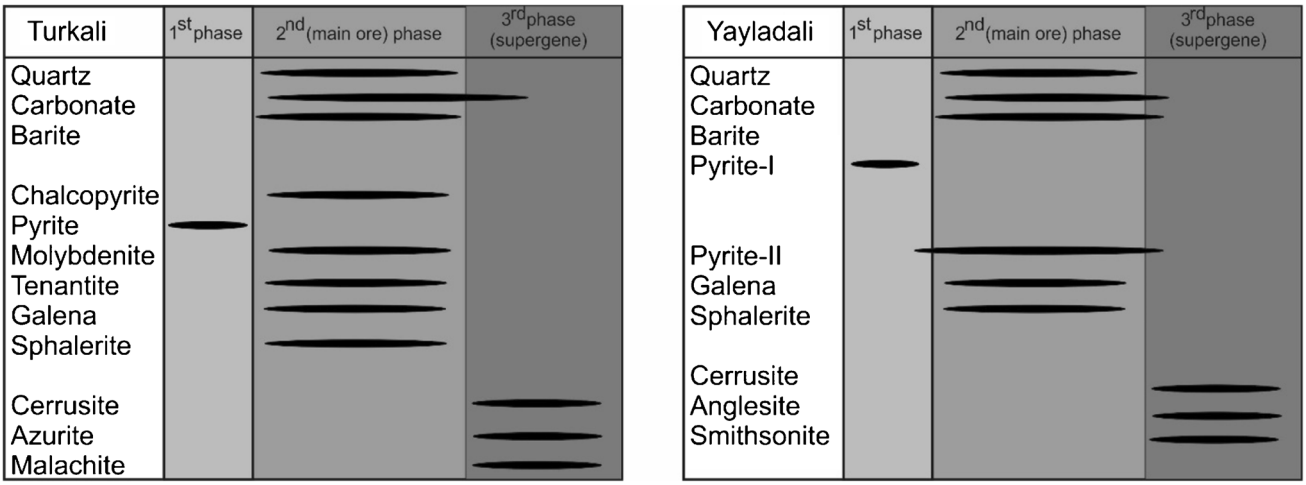


**Fig. 5** Paragenetic sequence of quartz, carbonate, and barite with sulfide minerals and supergene minerals as defined by mineral assemblages for Turkali and Yayladali ores

was completed by adding 6 ml of 5% boric acid solution to dissolve precipitated metal fluoride.

ELAN DRC-e Perkin Elmer model ICP-MS used this solution to analyze trace, REE, and PGEs. Fifteen ore samples were studied using DM4500P to reveal paragenesis sequences and ore texture. Fluid inclusion studies were conducted on 13 double-polished samples with minerals quartz, calcite, barite, and sphalerite minerals. The petrographical determinations were made on inclusions greater than 10 microns. The Linkam THMGS600 heating/freezing stage connected to a Leica microscope with a camera was used to obtain fluid inclusion data. The micro-thermometric data is recorded during the heating/freezing technique. Homogenization temperature is the minimum temperature of the fluid inclusion entrapped by the mineral in the heating experiment, and it is usually represented by Th. The temperatures

at which the last ice melt (Tmice) determine the freezing point of the fluid, and its value is used to determine the composition of the fluid (salinity). The salinity is determined according to Bodnar's Equation (1993).

$$\text{Salinity(wt.\%)} = 1.78\alpha - 0.0442\alpha 2 + 0.000557\alpha 3 \quad (\alpha = \text{Tmice})$$

where wt.% is the weight percent and Tmice is the temperature at which the last ice melted in degrees celsius (℃).

Hokieflics-H20-NaCl Excel sheet was used for the interpretation of fluid inclusion data. This Excel sheet was developed as a numerical tool to calculate P–V-T-X properties and trapping conditions of H2O-NaCl fluid inclusions by Steele-MacInnis et al. in 2012. Calculations on the program are based on the observed phase, the temperature of this phase that melts last and homogenization temperature data. Each calculation iterates for each single fluid inclusion. The salinity, density, pressure at homogenization, and dP/dT isochore slope are calculated for each fluid inclusion. (For the detailed explanations and detail behind the error corrections, please check Steele-MacInnis et al. 2012.)

## Results

### Mode of mineralization, petrography, and ore mineralogy

Two separate mineralization zones were identified in the study area. The Turkali granite-hosted Cu-Mo ± Au mineralization is located at the outward zones of Turkali pluton (N of Turkali village, Manisa) and has a significant resemblance to porphyry-type deposits. The granitoid is predominantly composed of quartz, K-feldspar, plagioclase, hornblende, and biotite (Fig. 3a–e).

Petrographic data show that the Turkali granitoid can be classified as a coarse-grained, plagioclase rich granodiorite with hornblende, biotite, and augite as mafic minerals. Due to the intense hydrothermal alteration process, the stockwork veins and brecciated zones are common within the granitoid body (Fig. 2f). Therefore, chlorite, calcite barite, and some opaque minerals are also observable (Fig. 3). The hydrothermal alteration types which observed in granite-hosted mineralization zones were identified as argillic (with kaolinite, smectite, and illite minerals) and phyllic (with fine-grained sericite, pyrite, and chlorite minerals) alterations.

The presence of chalcopyrite, molybdenite sphalerite, tennantite, and galena (Fig. 4a–e) indicates a porphyry-to-late stage overprinting; the hydrothermal system was active in Turkali granite-hosted mineralization field. In addition, the effect of weathering process can be concluded for the existence of supergene minerals such as anglesite, malachite, and azurite (Fig. 4a,d,e). The paragenetic relationships between gangue and ore minerals suggest three-phased mineralization at Turkali pluton-related mineralization (Fig. 5).

On the other hand, volcanic-hosted Yayladalı vein-type Pb–Zn ± Au ± Ag mineralization is situated approximately 33 km to Soma (Manisa) region, blocky pink to andesitic rocks belonging to the Yuntdagı Volcanics associated with volcanic breccias and stockworks host to the Pb–Zn ± Au ± Ag mineralization (Fig. 2a). The Pb–Zn occurrence was previously mined from a gallery of ~ 7 m in length in the district (Fig. 2b). The mineralizations in this region are found as vein/veinlets in the altered andesitic rocks. Thicknesses of these veins vary from 1 to 15 cm within argillic and chloritic alteration zones (Fig. 2c–f).

The medium-to-coarse-grained porphyritic andesites are composed of plagioclase (mostly andesine), amphibole (hornblende), biotite, and rarely sanidine phenocrysts in the study area. Accessory minerals such as apatite, zircon, rutile, sphene, and opaque minerals are observed in a microlithic groundmass. In some hydrothermally altered volcanic rocks, plagioclases are altered to sericite and epidote, and hornblendes and biotites to chlorite and fracture and veins are filled with recrystallized calcite (Fig. 3i,j,k). The volcanic-hosted mineralizations in the Yayladalı field were observed with argillic, phyllic, propyllitic, chloritic, silicic, and carbonate types of alterations. These alterations were possibly developed by a series of recurring hydrothermal pulses with significant base metal content.

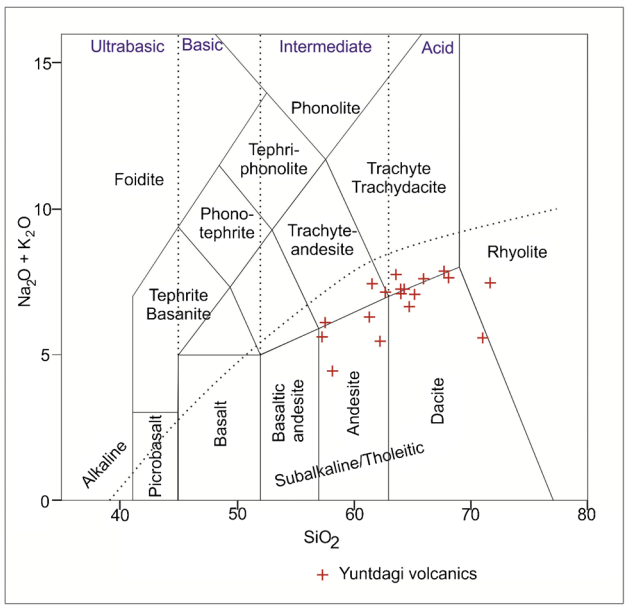


**Fig. 6** $SiO_2$ versus $Na_2O + K_2O$ diagram (using the classification scheme of Le Bas et al. 1986) showing the distribution of Yuntdagi volcanic (fresh rock geochemical data from; Ersoy et al. 2012)

The main ore formation styles are stockwork, and vein-type ore mineralizations occur as open-space filling in fracture, vein, and breccia within andesite in the study area. The vein type is 50-m long and 60-cm wide, dominated mainly by galena, pyrite, sphalerite quartz, and barite, whereas the stockworks are a mesh work of tiny veins 1-m long and 10-cm wide consisting of honey-colored and pale yellow sphalerite, galena, pyrite, chalcopyrite, barite, and calcite. Mineralogical composition is significantly dominated by massive sphalerite, galena, pyrite, and chalcopyrite, making up 90% of the ore minerals. Massive galenas are observed on the vein ore with triangular pits showing deformation structure (Fig. 4g).

The vein pyrites are corroded and partly replaced by hematites or associated with sphalerite and galena. Sphalerite is richer than galena at the stockwork and shows mutual association with galena replacing sphalerite on most of the ore samples, which might indicate contemporaneous deposition. The ore mineral paragenesis of Yayladali volcanic-hosted mineralization points out a three-phase sequence with quartz, carbonate barite as gangue minerals (Fig. 5). Most of the fluid inclusion types in the barite and sphalerite samples studied are primary and rare secondary inclusions. The sizes of inclusions range from 5 to 20 µm. The mineral assemblage indicates an intermediate sulphidation system in the Yayladali mineralization field.

## Geochemistry

Miocene West Anatolian volcanic rocks (WAVR) are andesite, latite, trachyte, dacite, and rhyolite, displaying orogenic signatures characterized by high K-calc-alkaline series (Ersoy et al. 2012). Their silica contents range between 45 and 70 (wt. %) and MgO content of < 9 (wt. %) with some leucite Miocene bearing dikes showing shoshonitic to ultrapotassic affinity (Akal 2013). Moreover, the geochemical data reveal a high LILE/HFSE ratio, high $^{87}Sr/^{86}Sr$, and low $^{143}Nd/^{144}Nd$ isotopic compositions, indicating subduction-related enriched mantle domains (Sayit and Göncüoglu 2009; Altunkaynak and Yilmaz 1999; Ersoy et al. 2012; Aldanmaz 2006).

The volcanic in the study area can be summarized as a calc-alkaline volcanic suite with rhyolites, dacites, and andesites according to the TAS diagram (Fig. 6). The geochemical data from the collected samples (Tables 1, 2, 3, 4, 5 and 6) and unaltered volcanic rock data from (Ersoy et al. 2012) were examined with the variation diagram (Fig. 7). Due to the intense alteration of both the granitic rocks of Turkali pluton and Yayladalı volcanic rocks, only the volcanic fresh rock geochemical data was used from Ersoy et al. (2012).

The geochemical data show positive trends for $Al_2O_3$, $K_2O$, $TiO_2$, and $P_2O_5$ vs. $SiO_2$ and negative trends for $Na_2O$, MgO, CaO, and $Fe_2O_3$ vs. $SiO_2$. These results for volcanic rocks indicate a fractionation process was active during the formation of Yuntdagi volcanic rocks. The negative trends of CaO and MgO alongside FeO can be interpreted as the fractionation of a hybrid magma chamber. It can be expected that the older parts of the volcanic sequence are more fractioned due to the active extensional tectonic regime in NW Turkey during the Eocene-Miocene period.

Geochemical signatures also suggest that crustal materials have possibly contaminated the magma due to the mixing of crustal or mantle magma or assimilation of the crustal material by the mantle-derived magma (Altunkaynak and Genç 2008). The mixing of mantle-derived magmas and lower crustal melts formed the main source of the primitive medium-to-high K-calc-alkaline rhyolite from the andesites (Ersoy et al. 2012). On the other hand, in mineralized volcanic samples, any correlation between $SiO_2$ with major oxides was not detected except for $SiO_2$ vs $K_2O$. This phenomenon likely occurred by the phyllic alteration observed with the sericitization of K-feldspar crystals.

The positive anomalies of large ion lithophile element (LILE) such as Ba, Rb, and K on mantle normalized trace element patterns (Fig. 8a) of unaltered Yuntdagi volcanic and least-altered Turkali granite sample points out that the post-collisional hybrid magma chamber had a significant incompatible element enrichment during fractionation the process. In addition, an important Pb anomaly is also observable, mostly caused by crustal contamination. The mineralized samples have more LILE enrichment and Pb anomalies, indicating that hydrothermal fluids also carried the mentioned elements alongside base metals.

The chondrite normalized REE (Fig. 8b) patterns in unaltered samples show enrichment in LREE and rather flat patterns in HREE, likely caused by the rather low interference of crustal contamination. The hydrothermally altered samples in both Turkali and Yayladali samples have lower LREE and HREE values, suggesting some of REEs may have remobilized during hydrothermal alteration stages. The positive Eu anomaly in hydrothermally altered rocks can be explained by the breakdown of Eu bearing plagioclase crystals, resulting in less mobile Eu ions enriched.

## Hydrothermal alteration

Major element variations are quantified to trace the intensity, fluid pathway, and depositional environment of hydrothermal alteration surrounding mineral deposits, especially in volcanogenic massive sulfide (VMS) (Ishikawa et al. 1976; Large et al. 2001a; Franklin and Gubins 1997). Most of the rocks around Yayladali (Soma region) are highly susceptible to weathering or secondary alteration processes. The

**Table 1** Major oxide analysis of Turkali pluton samples

| Sample | $SiO_2$ (%) | $Al_2O_3$ (%) | $Fe_2O_3$ (%) | MgO (%) | $Na_2O$ (%) | $K_2O$ (%) | CaO (%) | $TiO_2$ (%) | $P_2O_5$ (%) | MnO (%) | BaO (%) | LOI (%) | Total (%) |
|---|---|---|---|---|---|---|---|---|---|---|---|---|---|
| AB 1 | 63.7 | 14.4 | 6.80 | 1.16 | 0.17 | 0.55 | 0.34 | 0.51 | 0.14 | ND | 0.08 | 11.4 | 99.9 |
| AB2 | 61.6 | 15.0 | 5.84 | 2.15 | 2.12 | 2.69 | 4.42 | 0.61 | 0.21 | 0.05 | 0.13 | 5.13 | 99.9 |
| KB 1 | 72.2 | 11.5 | 3.98 | 0.14 | 5.82 | 0.49 | 0.38 | 0.43 | 0.06 | ND | ND | 2.71 | 99.9 |
| KB 2 | 70.4 | 2.83 | 3.33 | ND | 0.11 | 0.37 | 0.04 | 0.43 | 0.06 | ND | ND | 3.13 | 99.5 |
| KB 3 | 68.5 | 13.8 | 7.93 | 0.19 | 6.13 | 0.25 | 0.21 | 0.29 | 0.13 | 0.23 | 12.0 | 2.16 | 99.9 |
| KB 3A | 23.9 | 6.87 | 14.7 | 2.27 | ND | 0.02 | 26.6 | 0.14 | 0.03 | 0.23 | ND | 18.0 | 99.8 |
| KB-4A | 30.9 | 4.87 | 1.74 | 0.12 | 0.35 | 0.65 | ND | 0.15 | 0.04 | 0.26 | 37.3 | 3.62 | 98.8 |
| KB 4B | 48.8 | 25.1 | 11.3 | 0.85 | 0.04 | 3.16 | 0.08 | 0.62 | 0.345 | 0.01 | 0.16 | 8.31 | 99.3 |
| KB 5A | 74.6 | 11.8 | 2.22 | 0.17 | 0.10 | 7.05 | 0.07 | 0.41 | 0.12 | 0.01 | ND | 2.77 | 99.9 |
| KB 6A | 42.6 | 0.50 | 3.03 | ND | 0.01 | 0.06 | ND | 0.06 | ND | ND | 7.39 | 2.77 | 99.9 |
| KB 6B | 85.0 | 1.62 | 3.46 | ND | 0.04 | 0.21 | 0.04 | 0.20 | 0.04 | ND | 1.60 | 3.37 | 98.5 |
| KB 6C | 72.5 | 0.55 | 0.68 | ND | 0.13 | 0.04 | 0.08 | 0.03 | ND | ND | 12.1 | 3.08 | 98.0 |
| KB 6D | 64.0 | 0.78 | 2.93 | ND | 0.11 | 0.04 | 0.04 | 0.11 | 0.05 | ND | 10.8 | 5.45 | 99.7 |
| KB 7 | 64.5 | 21.1 | 0.24 | 0.26 | 7.82 | 1.37 | 0.79 | 1.22 | 0.02 | 0.01 | ND | 2.50 | 99.9 |
| KB 8 | 66.9 | 12.0 | 7.13 | 3.62 | 3.15 | 0.16 | 0.25 | 0.20 | 0.11 | 0.04 | ND | 4.45 | 99.9 |
| KB 10 | 66.8 | 16.3 | 3.62 | 1.59 | 5.09 | 1.11 | 0,29 | 0.41 | 0.23 | 0.02 | 0.14 | 3.67 | 99.9 |
| KB 11 | 57.0 | 15.1 | 5.64 | 2.56 | 5.44 | 0.33 | 0.40 | 0.36 | 0.18 | 0.05 | ND | 3.89 | 99.9 |
| KB 12 | 67.5 | 19.4 | 0.41 | 0.25 | 6.24 | 1.77 | 0.49 | 0.47 | 0.22 | ND | ND | 2.80 | 99.7 |
| KB 13A | 99.2 | 0.23 | 0.05 | ND | ND | 0.02 | 0.03 | ND | ND | ND | ND | 0.43 | 100.0 |
| KB 13B | 97.1 | 0.34 | 0.72 | 0.03 | ND | 0.09 | 0.05 | ND | 0.02 | 0.40 | ND | 1.10 | 99.9 |
| KB 14 | 80.1 | 7.22 | 3.81 | 0.24 | 0.62 | 4.87 | 0.46 | 0.31 | 0.34 | 0.02 | 0.15 | 1.40 | 99.9 |
| KB S | 61.4 | 19.4 | 4.59 | 1.10 | 5.72 | 0.95 | 0.52 | 0.60 | 0.49 | ND | 0.08 | 4.41 | 99.8 |
| KB-F | 71.9 | 9.95 | 6.28 | 0.47 | ND | 1.04 | 2.66 | 0.27 | 0.08 | 0.13 | ND | 5.64 | 99.5 |
| KBB V | 52.5 | 9.69 | 2.11 | 0.06 | 0.43 | 2.38 | 0.22 | 0.44 | 0.17 | ND | 0.10 | 21.2 | 99.9 |
| KBAG | 64.6 | 15.6 | 3.26 | 1.96 | 3.82 | 3.30 | 4.54 | 0.463 | 0.27 | 0.04 | 0.16 | 1.77 | 99.9 |
| KBQG | 88.2 | 2.53 | 6.45 | 0.07 | ND | 0.5 | 0.02 | 0.07 | 0.04 | ND | ND | 1.86 | 99.9 |

*ND*, not detected

**Table 2** Trace element analysis of Turkali pluton samples

| Sample | Zn (ppm) | Cu (ppm) | Nb (ppm) | Mn (ppm) | Mo (ppm) | Sr (ppm) | Rb (ppm) | Pb (ppm) | As (ppm) | Sb (ppm) | Ba (ppm) | Cs (ppm) | Th (ppm) | U (ppm) | Zr (ppm) | Au (ppb) | Ag (ppb) |
|---|---|---|---|---|---|---|---|---|---|---|---|---|---|---|---|---|---|
| AB 1 | 79 | ND | 9 | 34 | 5 | 262 | 26 | 55 | 42 | 2 | 597 | 3.52 | 21.3 | 4.54 | ND | 24 | ND |
| AB 2 | 116 | 38 | 11 | 395 | 2 | 275 | 62 | 39 | 0 | 1 | 1071 | 3.56 | 21.4 | 4.29 | 189.0 | 24 | ND |
| KB 1 | 6 | 21 | 10 | ND | 21 | 134 | 10 | 6 | 64 | 6 | 147 | 0.33 | 7.2 | 0.74 | 131 | 42 | 527 |
| KB 2 | 5 | 25 | 5 | ND | 57 | 596 | 10 | 11 | 131 | 392 | 107,042 | 3.52 | 1.5 | 0.47 | 66.0 | 117 | 2774 |
| KB 3 | 2 | 56 | 6 | ND | 15 | 191 | 6 | 15 | 55 | 8 | 219 | 0.32 | 7.9 | 0.93 | 89.0 | 23 | 561 |
| KB 3A | 394 | 5670 | 4 | 1796 | 3 | 581 | ND | 16 | 58 | 13 | 105 | 0.01 | 0.2 | 0.18 | 57.0 | 195 | 17,038 |
| KB 4A | 7432 | 23 | 4 | 2018 | 5 | 5761 | 15 | 29 | 25 | 31 | 333,477 | 2.50 | 1.2 | 0.96 | 107.0 | 39 | 1125 |
| KB 4B | 548 | 18 | 10 | 102 | 6 | 98 | 70 | 24 | 26 | 12 | 1220 | 5.29 | 14.8 | 2.91 | 140.0 | 33 | 484 |
| KB 5A | 66 | 28 | 8 | 39 | 9 | 64 | 167 | 30 | 175 | 63 | 2917 | 6.64 | 11.4 | 3.93 | 109.0 | 36 | 566 |
| KB 6A | 28,700 | 52 | ND | ND | 634 | 891 | 2 | 35 | 172 | 980 | 66,141 | 1.45 | ND | 1.59 | 306.0 | 234 | 49,738 |
| KB 6B | 311 | 107 | 3 | ND | 260 | 128 | 5 | 48 | 1597 | 826 | 14,320 | 3.08 | 7.65 | 1.07 | 68.0 | 289 | 12,559 |
| KB 6C | 1535 | 7 | 2 | ND | 43 | 733 | 1 | 65 | 2258 | 308 | 108,116 | 1.89 | ND | 0.26 | 30.0 | 82 | 1792 |
| KB 6D | 927 | 23 | 1 | ND | 489 | 835 | 1 | 73 | 3412 | 768 | 96,660 | 1.70 | 1.29 | 3.06 | 115.0 | 318 | 35,224 |
| KB 7 | 4 | 1 | 26 | 54 | 3 | 364 | 40 | 36 | 1613 | 1 | 169 | 0.55 | 11.4 | 10.4 | 206.0 | 81 | ND |
| KB 8 | 22 | 63 | 7 | 338 | 16 | 82 | 3 | 13 | 12 | 4 | 206 | 0.25 | 5.4 | 0.86 | 80.0 | 15 | ND |
| KB 10 | ND | 34 | 9 | 141 | 28 | 152 | 22 | 15 | 20 | 3 | 1058 | 0.89 | 16.0 | 0.73 | 108.0 | 22 | ND |
| KB 11 | 46 | 3610 | 8 | 358 | 34 | 199 | 7 | 27 | 35 | 15 | 69 | 0.60 | 15.2 | 4.86 | 121.0 | 26 | 3176 |
| KB 12 | ND | 2394 | 10 | ND | 4 | 245 | 31 | 7 | 12 | 4 | 405 | 2.05 | 26.9 | 2.94 | 128.0 | 11 | ND |
| KB 13A | 11,000 | ND | 2 | ND | 6 | 53 | ND | 4 | 4 | 201 | 17 | 0.26 | ND | ND | 14.0 | 27 | ND |
| KB 13B | ND | ND | 2 | 3098 | 6 | ND | ND | ND | ND | 239 | ND | 1.05 | ND | ND | 15.0 | 10 | ND |
| KB 14 | ND | 3 | 6 | 132 | 5 | 114 | 98 | 54 | 36 | 407 | 1142 | 7.26 | 7.71 | 0.72 | 76.0 | 15 | ND |
| KB S | ND | 228 | 12 | ND | 19 | 254 | 18 | 20 | 59 | 14 | 632 | 0.59 | 27.8 | 3.24 | 171.0 | 19 | ND |
| KB F | 326 | 786 | 8 | 1013 | 3 | 68 | 25 | 278 | 14 | 18 | 158 | 2.69 | 3.18 | 1.01 | 83.0 | 173 | 1452 |
| KBB V | ND | ND | 9 | ND | 5 | 451 | 6 | 221 | 10 | 7 | 769 | 0.46 | 17.3 | 5.02 | 162.0 | 24 | 325 |
| KBAG | 17,700 | 2 | 9 | 333 | 1 | 397 | 58 | 16 | ND | 1 | 1276 | 1.31 | 26.5 | 1.52 | 138.0 | 21 | ND |
| KBQG | ND | 271 | 3 | ND | 23 | 17 | 9 | 25 | 2 | 70 | 297 | 0.36 | ND | 0.08 | 29.0 | 332 | 8837 |

*ND*, not detected

**Table 3** REE analysis of Turkali pluton samples

| Sample | Y (ppm) | La (ppm) | Ce (ppm) | Pr (ppm) | Nd (ppm) | Sm (ppm) | Eu (ppm) | Gd (ppm) | Tb (ppm) | Dy (ppm) | Ho (ppm) | Er (ppm) | Tm (ppm) | Yb (ppm) | Lu (ppm) |
|---|---|---|---|---|---|---|---|---|---|---|---|---|---|---|---|
| AB 1 | 20.5 | 36.6 | 71.4 | 8.30 | 31.6 | 6.05 | 1.61 | 5.78 | 0.73 | 3.96 | 0.81 | 2.51 | 0.37 | 2.60 | 0.40 |
| AB 2 | 23.7 | 38.8 | 71.9 | 8.38 | 32.1 | 6.67 | 2.00 | 6.54 | 0.83 | 4.57 | 0.92 | 2.79 | 0.39 | 2.67 | 0.41 |
| KB 1 | 4.10 | 33.0 | 59.5 | 5.98 | 20.2 | 2.88 | 0.61 | 2.79 | 0.22 | 0.70 | 0.10 | 0.32 | 0.05 | 0.30 | 0.05 |
| KB 2 | 3.30 | 9.83 | 13.8 | 1.50 | 5.46 | 51.57 | 34.2 | 0.89 | 0.10 | 0.52 | 0.11 | 0.32 | 0.07 | 0.36 | 0.24 |
| KB 3 | 3.03 | 17.9 | 32.0 | 3.33 | 11.3 | 1.77 | 0.45 | 1.65 | 0.16 | 0.68 | 0.12 | 0.35 | 0.04 | 0.29 | 0.03 |
| KB 3A | 10.5 | 11.6 | 22.2 | 2.55 | 10.3 | 2.39 | 0.95 | 2.80 | 0.40 | 2.17 | 0.39 | 1.12 | 0.14 | 0.83 | 0.11 |
| KB 4A | 4.82 | 6.48 | 12.3 | 1.29 | 4.97 | 28.87 | 19.1 | 1.22 | 0.17 | 0.98 | 0.18 | 0.47 | 0.07 | 0.44 | 0.15 |
| KB 4B | 12.0 | 29.6 | 56.4 | 6.61 | 25.6 | 4.96 | 1.55 | 4.29 | 0.49 | 2.36 | 0.45 | 1.30 | 0.19 | 1.16 | 0.17 |
| KB 5A | 3.76 | 19.9 | 37.6 | 4.07 | 14.3 | 3.74 | 1.45 | 2.28 | 0.23 | 0.99 | 0.17 | 0.50 | 0.06 | 0.45 | 0.06 |
| KB 6A | 1.17 | 9.15 | 14.3 | 1.48 | 5.25 | 14.26 | 9.58 | 0.87 | 0.08 | 0.28 | 0.04 | 0.11 | 0.01 | 0.10 | 0.06 |
| KB 6B | 1.82 | 27.7 | 47.3 | 6.02 | 24.7 | 8.23 | 3.93 | 2.10 | 0.16 | 0.48 | 0.07 | 0.25 | 0.03 | 0.21 | 0.04 |
| KB 6C | 0.46 | 1.70 | 1.7 | 0.17 | 0.64 | 22.06 | 14.5 | 0.10 | 0.00 | 0.05 | 0.01 | 0.02 | 0.01 | 0.04 | 0.07 |
| KB 6D | 6.54 | 14.2 | 23.3 | 2.52 | 9.41 | 36.19 | 23.7 | 1.92 | 0.21 | 1.04 | 0.18 | 0.47 | 0.07 | 0.43 | 0.16 |
| KB 7 | 14.0 | 32.0 | 71.8 | 9.41 | 35.9 | 6.38 | 1.23 | 5.71 | 0.65 | 3.12 | 0.57 | 1.74 | 0.25 | 1.80 | 0.26 |
| KB 8 | 2.42 | 13.1 | 24.9 | 2.73 | 9.76 | 1.61 | 0.47 | 1.38 | 0.13 | 0.52 | 0.09 | 0.27 | 0.03 | 0.20 | 0.04 |
| KB 10 | 3.83 | 23.5 | 44.2 | 4.81 | 16.6 | 2.83 | 0.87 | 2.33 | 0.21 | 0.85 | 0.15 | 0.46 | 0.05 | 0.40 | 0.06 |
| KB 11 | 6.62 | 22.4 | 43.5 | 4.83 | 17.2 | 2.85 | 0.52 | 2.78 | 0.30 | 1.39 | 0.24 | 0.71 | 0.10 | 0.63 | 0.08 |
| KB 12 | 7.12 | 16.4 | 31.4 | 3.45 | 13.3 | 2.46 | 0.68 | 2.27 | 0.26 | 1.38 | 0.26 | 0.77 | 0.10 | 0.68 | 0.10 |
| KB 13A | 0.20 | 0.23 | 0.3 | 0.05 | 0.16 | 0.04 | 0.01 | 0.02 | ND | 0.02 | 0.01 | 0.02 | ND | 0.01 | ND |
| KB 13B | 0.89 | 1.65 | 2.3 | 0.22 | 0.81 | 0.24 | 0.09 | 0.21 | 0.03 | 0.21 | 0.04 | 0.11 | 0.01 | 0.08 | 0.01 |
| KB 14 | 4.14 | 11.7 | 24.1 | 2.89 | 11.1 | 2.39 | 0.75 | 1.78 | 0.20 | 0.91 | 0.17 | 0.47 | 0.06 | 0.36 | 0.05 |
| KB S | 7.65 | 61.0 | 105.2 | 10.9 | 37.3 | 5.84 | 1.73 | 5.23 | 0.49 | 1.80 | 0.29 | 0.89 | 0.10 | 0.66 | 0.09 |
| KB F | 7.00 | 15.6 | 30.0 | 3.41 | 12.4 | 2.42 | 0.64 | 2.48 | 0.29 | 1.45 | 0.27 | 0.74 | 0.09 | 0.64 | 0.08 |
| KBB V | 11.8 | 38.4 | 69.6 | 7.80 | 27.5 | 5.33 | 1.41 | 4.91 | 0.58 | 2.69 | 0.49 | 1.54 | 0.23 | 1.72 | 0.28 |
| KBAG | 15.1 | 36.5 | 64.0 | 7.42 | 25.9 | 4.97 | 1.42 | 4.67 | 0.56 | 2.82 | 0.55 | 1.67 | 0.23 | 1.51 | 0.21 |
| KBQG | 0.41 | 2.96 | 5.83 | 0.64 | 2.43 | 0.52 | 0.19 | 0.26 | 0.02 | 0.08 | 0.01 | 0.05 | 0.00 | 0.05 | 0.00 |

*ND*, not detected

depletion and enrichment of alkali elements (Na and K) and alkaline earth elements (Mg) are employed to delineate the different zones during hydrothermal activities. Sericite is represented by $K_2O$ formed by the destruction of feldspar and chlorite and $Fe_2O3$ and MgO due to the destruction of mostly hornblende and biotite in rocks (Ishikawa et al. 1976). However, the same approach is used to zone a stockwork and vein deposits hosted within andesitic volcanic rock using Eqs. (1) and (2) (Large et al. 2001b).

$$\text{Ishikawa alteration index(AI)}100 \times \left(K_2O + MgO\right) / K_2O + MgO + Na_2O + CaO \quad (1)$$

$$\text{chlorite carbonate pyrite index (CCPI)}100 \times \left(MgO + Fe_2O_3\right) / MgO + K_2O + Fe_2O_3 + Na_2O \quad (2)$$

Stockwork veins are generally found with a pale greenish chlorite-sericite-quartz zone, whitish sericite-quartz, and ore center with the chlorite-sericite-carbonate-pyrite zone. Veins demonstrated intense quartz-carbonate-barite and quartz-pyrite alteration zones. The vein gives AI values ranging from 23 to 66% in the quartz-pyrite-carbonate-barite zones. CCPI reveals 84 to 88% values in the greenish chlorite-sericite-quartz zone, 21 to 68% in the whitish-sericite-quartz zone, and 89 to 98% from toward the ore center with chlorite-sericite-carbonate-pyrite zone and barite zone. The vein shows CCPI values from 82 to 99% in the quartz-carbonate and quartz-pyrite zones. The concentrations of $Na_2O$ and CaO decreased in altered samples but increased 10 to 25% toward the ore center zone. The MgO, $Fe_2O_3$, and $K_2O$ ratio increases from distal zones toward the center from 6 to 7%, 11 to 22%, and 3.5 to 7%, respectively, indicating the intensity of chlorite and sericite alteration zones (Table 7). The alteration data of AI and CCPI are plotted on a box plot diagram (Fig. 9), separated by a diagonal line with the upper section, representing hydrothermal alteration and lower section diagenetic processes (Large et al. 2001b). All the samples plotted above the hydrothermal zone suggest a hydrothermal origin. Subtype 2 (Yayladali) occurred as massive ore bodies, quartz, and calcite; subtype 1 (Turkali) was mainly observed in the veins and stockworks. Quartz veins show comb and crustification structure with epizonal character in texture due to open-space mineralization. The Zn-Pb-$\pm$Au$\pm$Ag ore veins around the Yayladalı district in the southern part of the studied

**Table 4** Major oxide analysis of Yayladalı mineralization field samples

| Sample | $SiO_2$ (%) | $Al_2O_3$ (%) | $Fe_2O_3$ (%) | MgO (%) | $Na_2O$ (%) | $K_2O$ (%) | CaO (%) | $TiO_2$ (%) | MnO (%) | $P_2O_5$ (%) | LOI (%) | Total (%) |
|---|---|---|---|---|---|---|---|---|---|---|---|---|
| ML1 | 63.9 | 14.2 | 4.75 | 2.44 | 2.86 | 3.33 | 5.07 | 0.61 | 0.04 | 0.23 | 2.31 | 99.8 |
| ML2 | 20.0 | 3.71 | 19.2 | 3.9 | ND | 0.05 | 23.3 | 0.13 | 1.50 | 0.06 | 14.0 | 99.9 |
| ML3 | 24.3 | 3.11 | 22.5 | 4.68 | ND | 0.16 | 12.7 | 0.05 | 7.36 | 0.02 | 24.8 | 99.9 |
| ML4 | 57.2 | 17.7 | 4.05 | 2.11 | 0.14 | 7.19 | 2.71 | 0.63 | 0.11 | 0.25 | 6.94 | 99.9 |
| ML5A | 53.3 | 15.6 | 12.3 | 6.00 | 0.03 | 3.14 | 0.25 | 0.54 | 0.36 | 0.19 | 6.16 | 99.9 |
| ML5B | 63.2 | 7.96 | 10.9 | 0.60 | 0.05 | 1.25 | 1.50 | 0.20 | 1.70 | 0.13 | 7.45 | 99.9 |
| ML6A | 43.7 | 5.86 | 7.77 | 0.49 | 0.12 | 1,51 | 2.02 | 0.13 | 0.60 | 0.07 | 8.85 | 99.9 |
| ML6B | 92.4 | 1.95 | 0.87 | 0.15 | 0.01 | 0.31 | 0.03 | 0.04 | 0.03 | 0.02 | 1.58 | 100.0 |
| ML7 | 56.9 | 14.7 | 12.2 | 0.52 | 0.13 | 5.22 | 0.10 | 0.47 | 0.01 | 0.23 | 8.85 | 99.9 |
| ML8 | 64.9 | 18.8 | 1.77 | 0.70 | 1.16 | 7.21 | 0.23 | 0.62 | 0.01 | 0.26 | 4.00 | 99.9 |
| ML9 | 38.3 | 6.48 | 6.84 | 2.09 | ND | 0.82 | 5.50 | 0.17 | 0.52 | 0.06 | 10.0 | 99.8 |
| ML10 | 45.7 | 1.33 | 3.96 | 6.88 | ND | 0.34 | 16.0 | 0.03 | 1.05 | 0.02 | 15.9 | 99.9 |
| ML11 | 61.6 | 15.8 | 5.35 | 3.63 | 2.43 | 6.03 | 0.58 | 0.58 | 0.11 | 0.28 | 3.21 | 99.8 |
| ML12 | 29.1 | 8.71 | 15.0 | 2.57 | 0.69 | 1.25 | 8.37 | 0.25 | 1.32 | 0.09 | 14.7 | 99.8 |
| ML 13 | 62.1 | 15.8 | 5.31 | 2.97 | 2.51 | 6.00 | 0.53 | 0.56 | 0.20 | 0.26 | 3.18 | 99.8 |
| ML 14 | 66.6 | 19.6 | 1.48 | 0.57 | 1.98 | 4.37 | 0.19 | 0.61 | ND | 0.05 | 4.35 | 99.9 |
| ML 15 | 80.4 | 6.96 | 3.54 | 0.07 | 0,02 | 0.05 | 0.04 | 0.07 | 0.14 | 0.05 | 3.81 | 99.9 |
| ML16 | 26.02 | 1.06 | 6.60 | 4.52 | ND | 0.17 | 15.5 | 0.03 | 1.93 | ND | 14.2 | 99.7 |
| MLG1 | 13.75 | 6.30 | 18.3 | 5.71 | ND | 0.25 | 12.5 | 0.13 | 1.62 | 0.06 | 15.2 | 99.9 |
| MLG2 | 7.36 | 2.49 | 22.5 | 5.93 | ND | 0.33 | 13.7 | 0.04 | 1.44 | 0.03 | 14.0 | 99.9 |
| MLG3 | 2.05 | 1.17 | 8.95 | 7.72 | 0.01 | 0.15 | 24.6 | ND | 2.99 | ND | 13.0 | 99.9 |
| MLG4 | 25.3 | 11.05 | 18.97 | 7.15 | ND | 0.05 | 10.8 | 0.31 | 1.48 | 0.12 | 16.18 | 99.9 |

*ND*, not detected

**Table 5** Trace element analysis of Yayladalı mineralization field samples

| Sample | Zn (ppm) | Cu (ppm) | Nb (ppm) | Mn (ppm) | Mo (ppm) | Sr (ppm) | Rb (ppm) | Pb (ppm) | As (ppm) | Sb (ppm) | Ba (ppm) | Cs (ppm) | Th (ppm) | U (ppm) | Zr (ppm) | Au (ppb) | Ag (ppb) |
|---|---|---|---|---|---|---|---|---|---|---|---|---|---|---|---|---|---|
| ML1 | 130 | 25 | 11 | 317 | 2 | 427 | 77 | 30 | 32 | 2 | 814 | 6.3 | 20.6 | 2.2 | 164 | 24 | ND |
| ML2 | 23,100 | 12 | 2 | 11,583 | 3 | 505 | 3 | 5459 | 576 | 407 | 24,255 | 0.7 | 3.2 | 0.8 | 54 | 310 | 14,863 |
| ML3 | 443 | 32 | 2 | 56,695 | 2 | 96 | 10 | 38 | 68 | 22 | 33 | 1.9 | 1.5 | 0.4 | 30 | 23 | ND |
| ML4 | 15,800 | 4 | 10 | 879 | 1 | 104 | 227 | 109 | 72 | 10 | 1487 | 11.2 | 20.2 | 3.4 | 154 | 35 | ND |
| ML5A | 1695 | 33 | 9 | 2740 | 3 | 25 | 97 | 6963 | 116 | 8 | 371 | 13.2 | 13.9 | 3.4 | 142 | 97 | 10,742 |
| ML5B | 10,470 | 22 | 5 | 13,096 | 5 | 50 | 53 | 172 | 287 | 41 | 378 | 8.3 | 8.4 | 1.9 | 87 | 123 | 4867 |
| ML6A | 17,800 | 29 | 4 | 4600 | 2 | 29 | 62 | 658 | 40 | 35 | 918 | 3.8 | 5.0 | 4.0 | 83 | 170 | 7193 |
| ML6B | 9414 | 5 | 3 | 216 | 2 | 27 | 13 | 186 | 53 | 54 | 1617 | 1.2 | 1.0 | 0.4 | 26 | 25 | 1571 |
| ML7 | 2958 | 6 | 9 | 105 | 2 | 57 | 152 | 594 | 131 | 20 | 1176 | 9.6 | 16.3 | 6.1 | 138 | 25 | 785 |
| ML8 | 399 | 5 | 12 | 40 | ND | 142 | 200 | 34 | 42 | 6 | 1686 | 9.6 | 21.0 | 4.4 | 166 | 23 | ND |
| ML9 | 11,620 | 34 | 7 | 4027 | 114 | 969 | 28 | 3252 | 67 | 13 | 40,991 | 13.1 | 4.9 | 0.9 | 80 | 145 | 2924 |
| ML10 | 45,900 | 6 | 2 | 8052 | 3 | 81 | 10 | 4540 | 37 | 20 | 690 | 8.3 | 0.4 | 0.1 | 36 | 14 | 2764 |
| ML11 | 71,300 | 5 | 9 | 861 | 3 | 252 | 171 | 111 | 28 | 5 | 2003 | 0.8 | 18.5 | 3.0 | 154 | 15 | ND |
| ML12 | 13,000 | 21 | 5 | 10,139 | 5 | 396 | 47 | 876 | 121 | 27 | 19,780 | 7.9 | 8.6 | 1.6 | 148 | 103 | 16,889 |
| ML 13 | 11,000 | 6 | 11 | 1535 | 2 | 312 | 197 | 440 | 35 | 8 | 1879 | 5.3 | 19.3 | 4.1 | 156 | 17 | ND |
| ML 14 | 499 | 7 | 10 | ND | 2 | 87 | 104 | 19 | 25 | 7 | 627 | 8.2 | 19.6 | 3.8 | 142 | 18 | ND |
| ML 15 | 9800 | 1 | 3 | 1074 | 6 | 12 | 2 | 12,400 | 42 | 60 | 4010 | 9.6 | 2.2 | 1.1 | 660 | 18 | 14,177 |
| ML 16 | 50,200 | 25 | ND | 14,848 | 2 | 1462 | 10 | 11,254 | 360 | 36 | 11,0801 | 1.7 | 0.1 | 0.2 | 44 | 1151 | 5429 |
| ML G1 | 14,970 | 136 | 5 | 12,482 | 26 | 216 | 8 | 50 | 104 | 4 | 4224 | 3.1 | 1.1 | 0.3 | 49 | 28 | ND |
| ML G2 | 18,820 | 60 | 1 | 11,054 | 14 | 163 | 6 | 152 | 39 | 3 | 4068 | 1.1 | 0.3 | 2.0 | 22 | 24 | 1168 |
| ML G3 | 23,540 | 33 | 4 | 23,028 | 3 | 232 | 9 | 9461 | 45 | 4 | 235 | 2.9 | 0.0 | 0.1 | 25 | 141 | 2213 |
| ML G4 | 50,700 | 367 | 5 | 11,363 | 15 | 112 | 2 | 379 | 127 | 7 | 157 | 1.0 | 3.5 | 0.5 | 94 | 71 | 526 |

*ND*, not detected

**Table 6** REE analysis of Yayladalı mineralization field samples

| Sample | Y (ppm) | La (ppm) | Ce (ppm) | Pr (ppm) | Nd (ppm) | Sm (ppm) | Eu (ppm) | Gd (ppm) | Tb (ppm) | Dy (ppm) | Ho (ppm) | Er (ppm) | Tm (ppm) | Yb (ppm) | Lu (ppm) |
|---|---|---|---|---|---|---|---|---|---|---|---|---|---|---|---|
| ML 1 | 15.4 | 35.6 | 67.4 | 7.73 | 28.5 | 5.30 | 1.30 | 4.86 | 0.60 | 3.17 | 0.58 | 1.69 | 0.24 | 1.54 | 0.24 |
| ML 2 | 20.9 | 7.42 | 17.1 | 2.59 | 13.0 | 10.6 | 9.34 | 6.49 | 0.72 | 3.66 | 0.51 | 1.18 | 0.13 | 0.82 | 0.14 |
| ML3 | 13.6 | 6.23 | 11.9 | 1.59 | 7.40 | 2.57 | 2.50 | 3.42 | 0.49 | 2.43 | 0.37 | 0.81 | 0.09 | 0.53 | 0.07 |
| ML 4 | 12.9 | 34.4 | 67.7 | 7.63 | 28.7 | 5.49 | 1.70 | 4.54 | 0.51 | 2.60 | 0.50 | 1.46 | 0.20 | 1.39 | 0.20 |
| ML 5A | 11.2 | 25.7 | 47.6 | 5.52 | 20.3 | 3.49 | 0.98 | 3.28 | 0.36 | 1.80 | 0.36 | 1.04 | 0.15 | 1.03 | 0.15 |
| ML6A | 22.5 | 13.1 | 25.2 | 3.25 | 13.6 | 4,15 | 2.22 | 5.27 | 0.93 | 3.72 | 0.58 | 1.43 | 0.16 | 1.01 | 0.17 |
| ML6B | 1.98 | 2.99 | 5.73 | 0.62 | 2.40 | 0.98 | 0.54 | 0.48 | 0.07 | 0.39 | 0.07 | 0.17 | 0.02 | 0.15 | 0.02 |
| ML7 | 9.46 | 22.9 | 39.8 | 4.47 | 16.2 | 3.06 | 1.08 | 2.60 | 0.32 | 1.71 | 0.34 | 1.01 | 0.15 | 1.03 | 0.16 |
| ML8 | 10.8 | 32.7 | 62.6 | 7.01 | 26.1 | 4.68 | 1.30 | 3.97 | 0,43 | 2,19 | 0.41 | 1.30 | 0.18 | 1.26 | 0,20 |
| ML9 | 10.9 | 11.7 | 20.9 | 2.34 | 9.12 | 10.0 | 6.66 | 2.69 | 0.40 | 2.09 | 0.38 | 1.02 | 0.12 | 0.75 | 0.15 |
| ML10 | 6.75 | 5.80 | 8.03 | 1.13 | 4.54 | 1.23 | 1.42 | 1.30 | 0.17 | 0,92 | 0,16 | 0.36 | 0.05 | 0.29 | 0.04 |
| ML11 | 13.7 | 31.0 | 61.0 | 6.81 | 25.2 | 4.91 | 1.84 | 4.22 | 0.49 | 2.86 | 0.51 | 1.54 | 0.21 | 1.46 | 0.20 |
| ML 12 | 24.1 | 25.3 | 45.2 | 5.60 | 22.5 | 10.6 | 8.00 | 6.57 | 0.92 | 4.66 | 0.77 | 1.93 | 0.23 | 1.46 | 0.22 |
| ML 13 | 13.3 | 32.8 | 62.1 | 7.07 | 25.9 | 5.12 | 1.82 | 4.29 | 0.52 | 2.73 | 0.54 | 1.57 | 0.21 | 1.51 | 0.22 |
| ML 14 | 9.24 | 29.0 | 54.6 | 6.05 | 22.1 | 3.96 | 1.04 | 3.21 | 0.35 | 1.86 | 0.36 | 1.14 | 0.17 | 1.28 | 0.21 |
| ML 15 | 22.8 | 2.97 | 8.75 | 1,37 | 7.24 | 4.05 | 3.89 | 4.14 | 0.70 | 3.93 | 0.61 | 1.36 | 0.20 | 0.94 | 0.10 |
| ML16 | 18.9 | 5,02 | 9.34 | 1.47 | 7.90 | 13.0 | 9.35 | 5.08 | 0.75 | 3.58 | 0.55 | 1.14 | 0.12 | 0.70 | 0.14 |
| MLG1 | 18.9 | 12.3 | 23.5 | 2.79 | 11.4 | 4.54 | 5.41 | 4.89 | 0.72 | 3.59 | 0.57 | 1.27 | 0.15 | 0.87 | 0.11 |
| MLG2 | 14.1 | 5.42 | 10.3 | 1.27 | 5.63 | 2.94 | 2.61 | 2.94 | 0.49 | 2.70 | 0.42 | 0.99 | 0.11 | 0.71 | 0.10 |
| ML G3* | 41.2 | 27.5 | 46.6 | 5.90 | 26.4 | 8.68 | 14.1 | 11.5 | 1.61 | 7.55 | 1.06 | 2.27 | 0.24 | 1.37 | 0.18 |
| ML G4 | 19.3 | 23.9 | 44.8 | 5.19 | 20.3 | 4.94 | 4.60 | 5.97 | 0.79 | 3.79 | 0.61 | 1.35 | 0.15 | 0.87 | 0.12 |

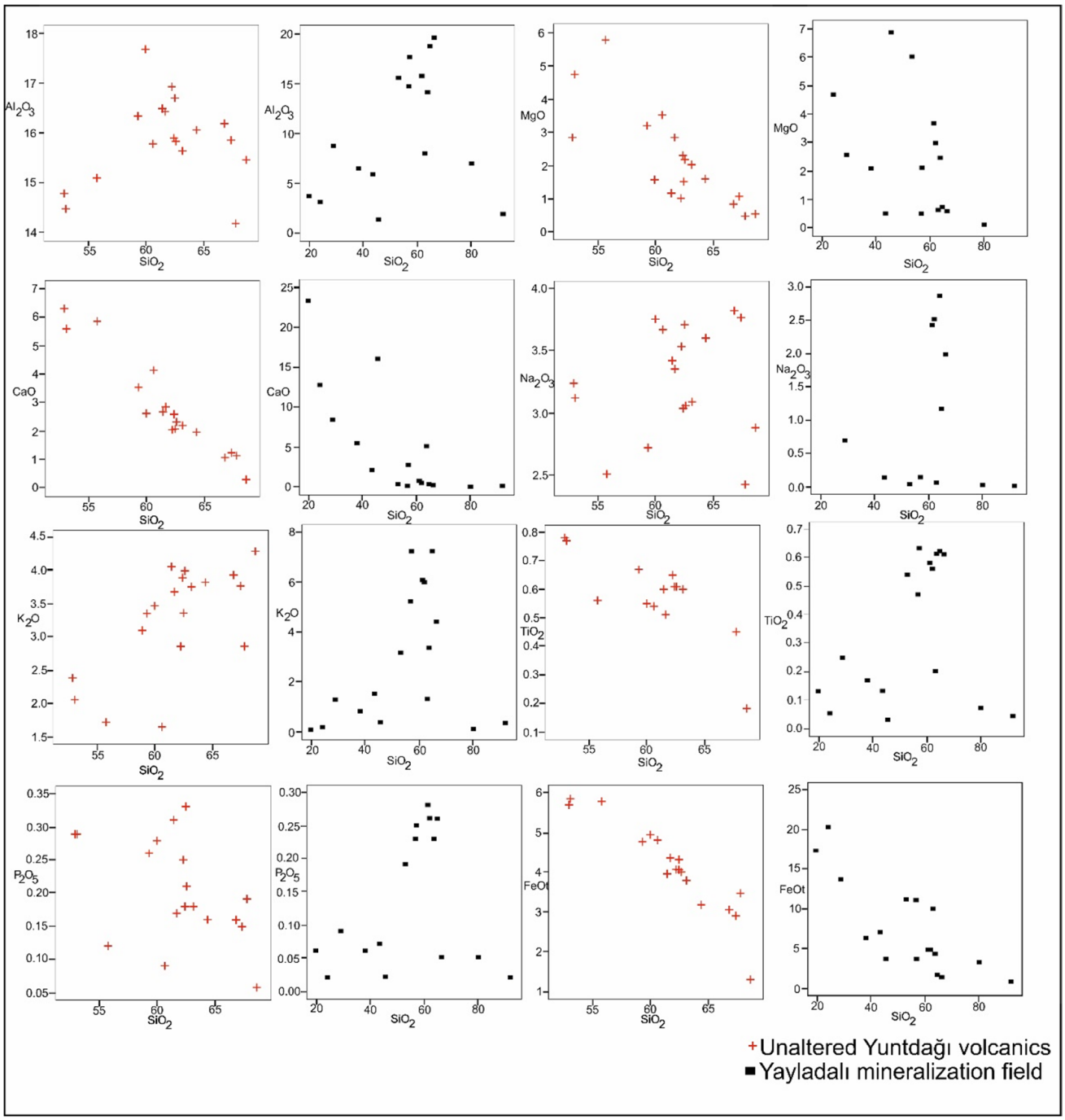


**Fig. 7** Major element trends of unaltered Yuntdağı volcanic (data from Ersoy et al. 2012) and Yayladalı mineralization field

area show evidence of three paragenetic sequences for mineralizations. Pre-mineralization deposition of framboidal pyrites and quartz followed by faulting and brecciation to main ore mineralization stage of other sulfides. Sulfide phases such as sphalerite, galena, chalcopyrite, and tennantite in open-space fracture are replaced with cubic pyrite, barite, hydrothermal quartz, calcite with cerussite, smithsonite, hematite, and anglesite in later mineralization stage.

## Characteristics of fluid inclusions

Sphalerite-galena sulfide ore samples from veins were used to obtain the relationship between the host rock and

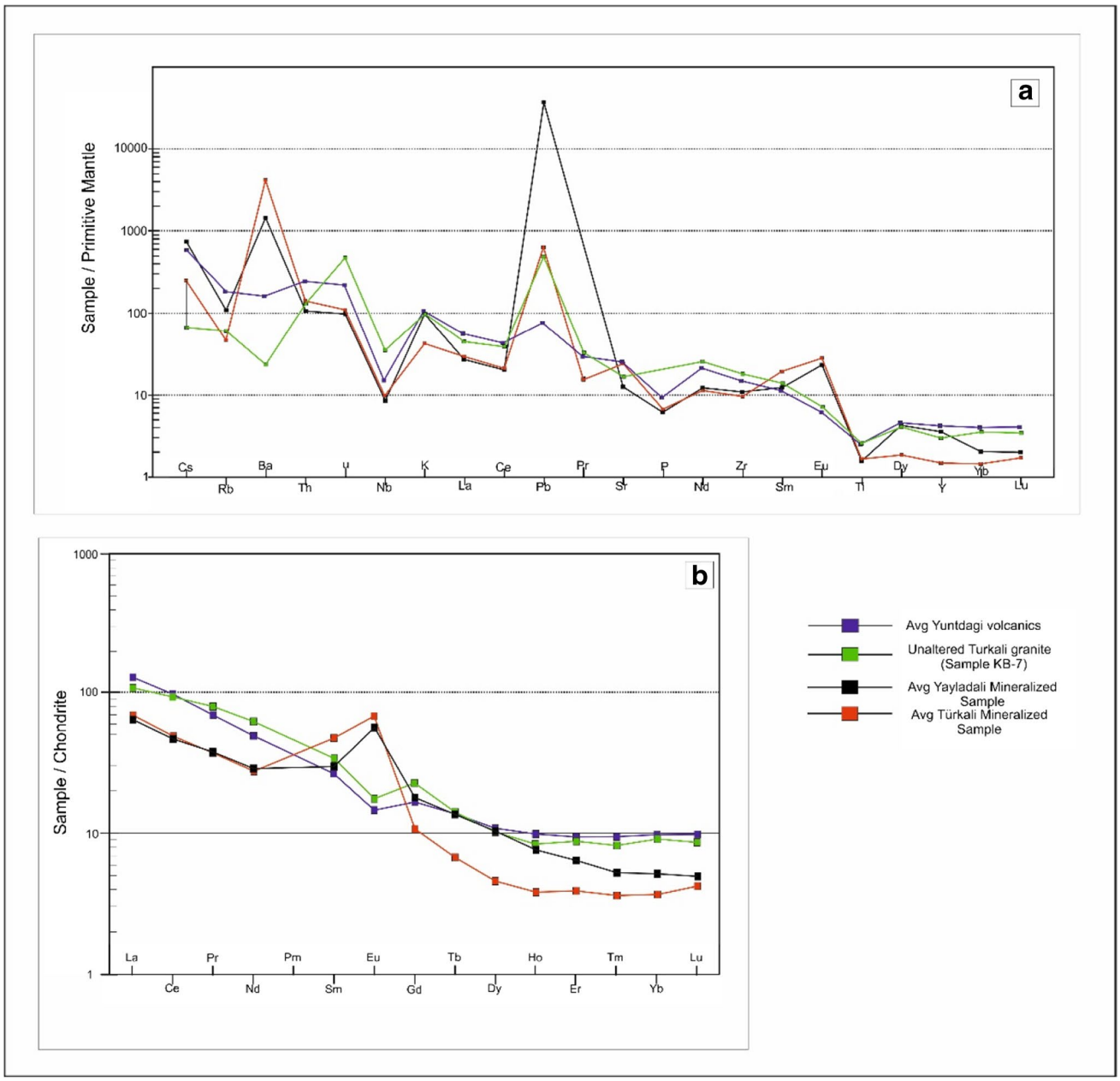


**Fig. 8** (**a**) Primitive mantle (Sun and McDonough, 1989) normalized trace element and (**b**) chondrite normalized (Boynton 1984) REE patterns of study area rocks (Avg Yuntdagi data were obtained from Ersoy et al. 2012)

the mineralization corresponding fluid inclusions. Fluid inclusion studies of these samples were characterized by quartz, calcite, barite, and sphalerite. To this end, 13 double-polished sections of quartz, calcite, barite, and sphalerite samples were used, and observations were iterated for 28 different fluid inclusion from these samples. The aim of this study here is to determine the ore formation conditions such as temperature, density, and salinity of the entrapped fluid.

Fluid inclusions are classified as primary, secondary, or pseudo secondary if they are formed as a result of growth around crystals during fracture healing or formed by fracture during crystal growth, respectively (Roedder 1984; Goldstein et al. 2003). According to the genetic classification of Roedder (1984), the inclusions in the studied samples are primary (P) and rare secondary (S) in character and have varying shapes and sizes.

**Table 7** Calculated values for AI and CCPI for Turkali (KB) and Yayladali (ML) samples

| Sample | AI (%) | CCPI (%) | Sample | AI (%) | CCPI (%) |
|---|---|---|---|---|---|
| AB 1 | 76.5 | 90.9 | **ML1** | 42.1 | 52.0 |
| AB2 | 42.5 | 60.6 | **ML4** | 76.6 | 44.0 |
| KB 1 | 9.16 | 37.3 | **ML5A** | 97.1 | 84.3 |
| KB 3 | 6.58 | 53.4 | **ML5B** | 54.3 | 88.9 |
| KB 4B | 97.1 | 77.4 | **ML6A** | 48.2 | 82.1 |
| KB 5A | 97.8 | 23.3 | **ML6B*** | 92.8 | 74.8 |
| KB 7 | 16.0 | 4.91 | **ML7** | 96.2 | 68.3 |
| KB 8 | 52.8 | 75.2 | **ML8** | 85.1 | 21.6 |
| KB 10 | 33.4 | 43.9 | **ML10** | 31.1 | 97.0 |
| KB 11 | 33.1 | 57.0 | **ML11** | 76.2 | 49.9 |
| KB 12 | 23.1 | 7.21 | **ML12** | 29.7 | 89.2 |
| KB 14 | 82.5 | 40.0 | **ML 13** | 74.8 | 47.7 |
| KB S | 24.8 | 44.0 | **ML 14** | 69.5 | 23.0 |
| KBB V | 78.9 | 41.0 | **ML 15** | 66.4 | 98.0 |
| KBAG | 38.6 | 40.7 | | | 52.0 |

Micro-thermometry studies were conducted mostly on primary fluid inclusions because they are formed around crystal growth and likely reflect the genetic formation conditions. Primary quartz inclusions are mainly perpendicular to the euhedral quartz crystal faces. Sphalerite inclusions are bright and yellowish, while quartz and barite are colorless (Fig. 10c). The bright colors reveal a high aqueous density fluid of water, and others are dark due to a low refractive index of carbon dioxide liquids (Van den Kerkhof and Hein 2001).

The sizes of inclusions range from 5 to 40 µm. The dominant morphology of the fluid inclusions encountered is elongated or negative crystal shapes. A significant fraction of the fluid inclusions is greater than 10 µm, even if some of them are less than it. The shape of the inclusion ranges from rounded to globules and some elongated (Fig. 10a,b). The main inclusions recognized are type I (liquid + vapor), type II (liquid + vapor + $CO_2$ vapor), and type III (liquid + vapor + $CO_2$ vapor + solid).

Types of fluid inclusions and their genetic features are summarized in Table 8. The L/V volume ratio varied from 90 to 70%, where inclusions are elongated more; they show a variable L-V ratio, and in some sphalerite, samples appear

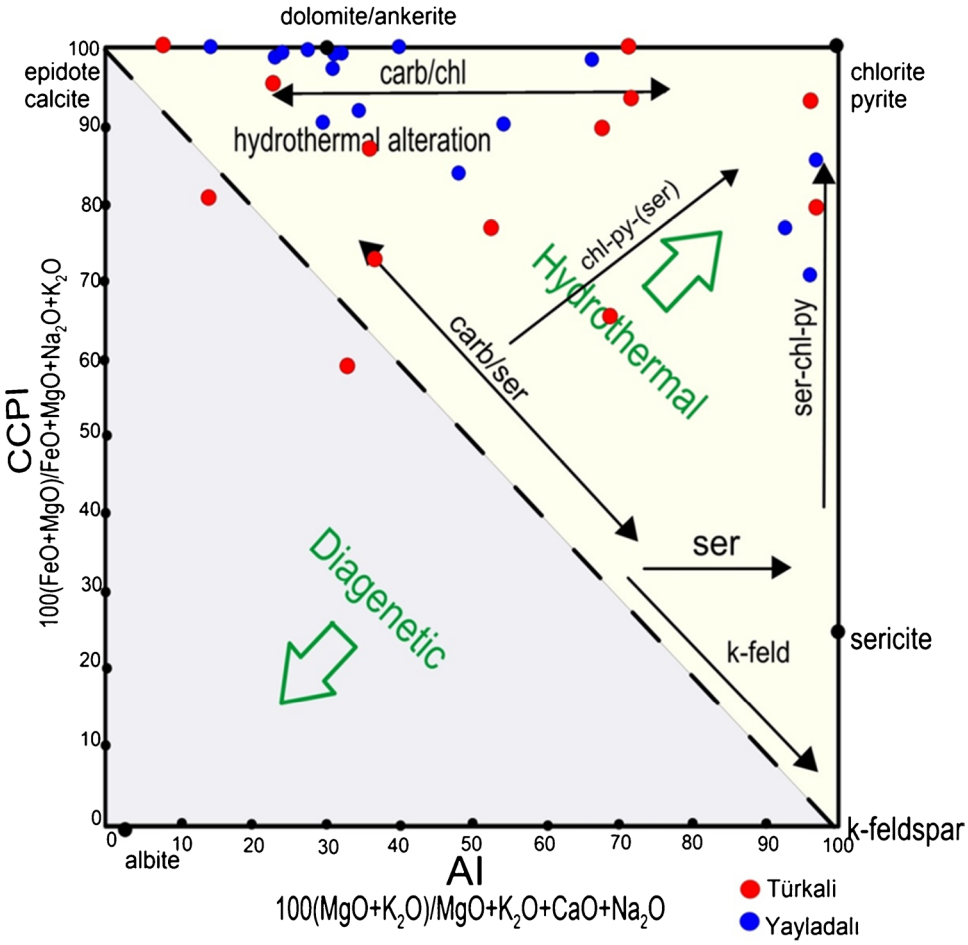


**Fig. 9** Samples alteration pattern on AI-CCPI box plot diagram (modified after Large et al. 2001a, b)

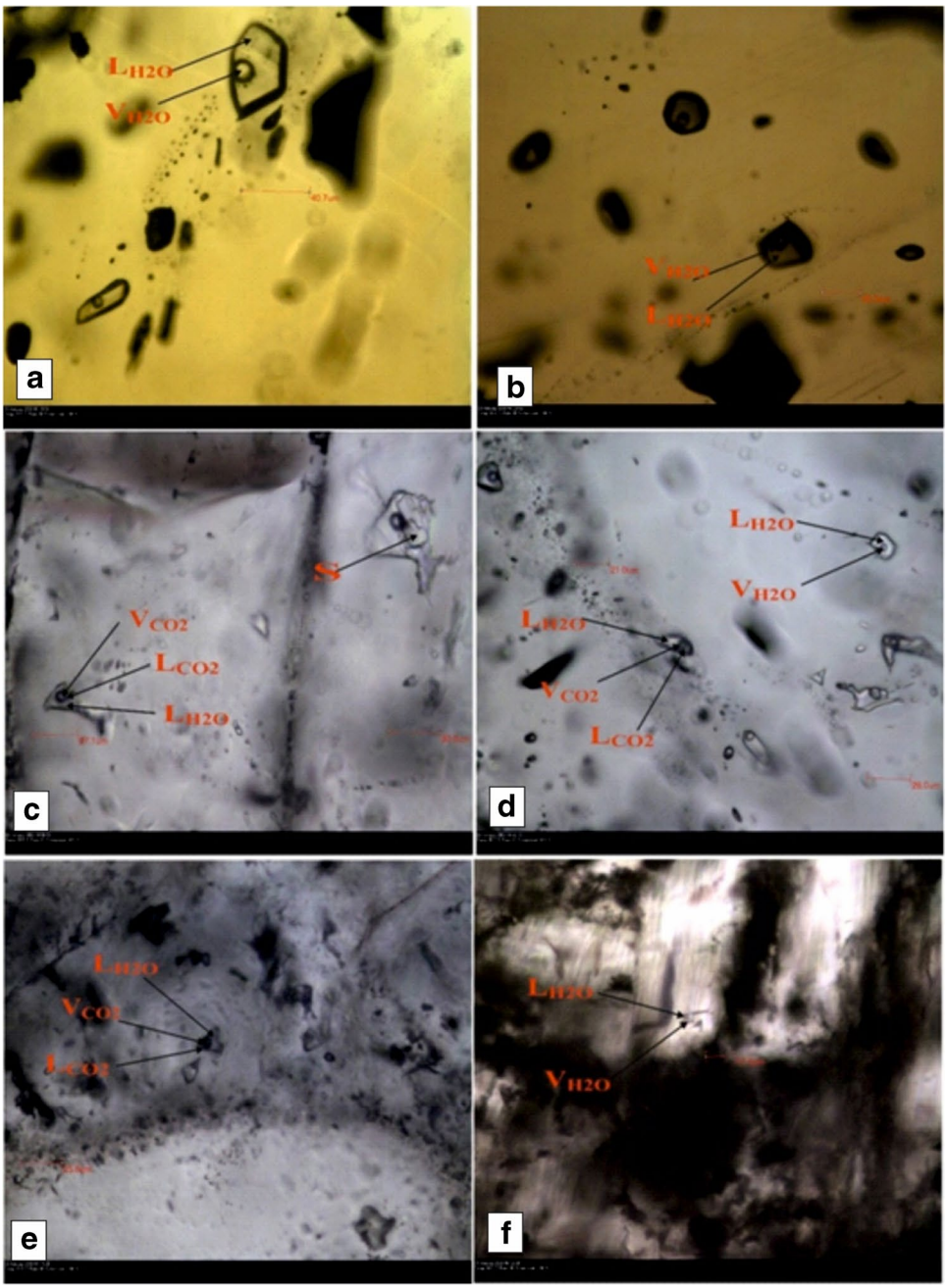


**Fig. 10** Photomicrograph of ore mineral assemblages and specific fluid inclusions. (**a**) Liquid phase (LH2O) and vapor phase (VH2O) in sphalerite. (**b**) Some different types of fluid inclusion assemblages (FIA). (**c**) Scale of the low refractive index of liquids. (**d**) Tensional effects and decrepitation of fluid inclusions

to stretch as a result of volume change without loss of materials (Fig. 10d). Daughter minerals are not seen in fluid inclusions.

## Micro-thermometry of fluid inclusions

Type I and type II generations were micro-thermometry analyzed because they are part of the fluid inclusion assemblages (FIA). Type III and some others formed around heal microcracks crosscutting crystal boundaries were not evaluated because they are the later generations or not concerned a part of FIA. The micro-thermometric data for both primary and secondary inclusions were recorded, emphasizing the primary inclusion measurements from quartz, barite, and sphalerite.

However, very few samples hosted an appreciable amount of measure fluid inclusions. Individual measurements of various fluid inclusions with varied characteristics were obtained and not the average. The spatial distribution of primary inclusion suggests that entrapment of the fluid inclusions occurs during specific stages in the growth of the crystals. In all

**Table 8** Summary of fluid inclusion types, morphology, and phases present at 25 ℃

| Type | Subtype | Inclusion shape | Size (μm) | Number of Phases | L/V ratio[1] | Types[2] |
|---|---|---|---|---|---|---|
| I | a | Negative crystals | < 5–40 | 4–5 | 90–80/10–20 | Liquid + vapor |
| | b | Elongate | < 5–30 | 4–5 | 90–70/10–30 | Liquid + vapor |
| | c | Rounded | < 5–20 | 3–4 | 80–70/20–30 | Liquid + vapor |
| | d | Globule | ~ 20 | 1–2 | 80/20 | Liquid + vapor |
| | e | Irregular | ~ 20 | 1–2 | 80/20 | Liquid + vapor |
| II | a | Negative crystals | < 20–30 | 2–3 | 80/20 | Liquid + vapor ($H_2O + CO_2$) |
| | b | Elongate | < 5–20 | 4–6 | 90–70/10–30 | Liquid + vapor ($H_2O + CO_2$) |
| | c | Irregular | < 10–20 | 3–4 | 90/10 | Liquid + vapor ($H_2O + CO_2$) |
| III | a | Negative crystals | ~ 35 | 1 | 55–10 (35 solid) | Liquid + vapor ($H_2O + CO_2$) + halite |

[1]Observations about L/V ratios are based onKlyukin et al. (2019)

[2]Solely liquid and vapor terms are defining $H_2O$

measured fluid inclusions, the vapor phase shrinks progressively during heating; this implies that they are not homogenized with the liquid phase. The measurements from the secondary fluid inclusions give a homogenization temperature of less than 150 ℃, which may also represent another episode of the primary fluid inclusions within the quartz and sphalerite crystals that range from 192 to 280 ℃.

The homogenization temperatures (Th), last ice melting temperatures, salinity, and densities are summarized and illustrated in (Table 2). Combing the homogenization temperature (Th) and fluid salinity contours gives fluid density by equal density lines (Brown 1989). The density varies from 0.794 to 1.056 g/cm$^3$. Fluid inclusions of primary quartz veins from the study area show Th ranging between 204 and 264 ℃, sphalerite 192 and 251 ℃, and barite 208 and 280 ℃. Fluid inclusion studies on sphalerite, quartz, barite, and calcite veins give high salinity fluid (2.4–15.47 wt.% and 5.86–17.96 wt.%) with corresponding high homogenization temperature (197.5–280.1 ℃ and 191.5–250.1 ℃) for Turkali and Yayladali, respectively (Table 9).

These parameters are favorable for the mineralization/precipitation/deposition of more base metals like Zn-Pb which are usually transported as chloride complexes and indicate an intermediate epithermal sulphidation vein-type mineralization (Bodnar et al. 2014). However, as a controversy in the Turkali region, high salinity measured only with high-temperature data indicates a high sulphidation mineralization style additionally to the intermediate sulphidation mineralization style in the region (Bodnar et al. 2014 and references therein for the implications originating from characteristics of IS- and HS-type deposits). The fluid density and trend likely indicate boiling as the main physical process responsible for ore fluid precipitation with a trace of influence by fluid mixing (Figs. 11 and 12).

**Table 9** Calculated values of salinity and homogenization temperature (Th) during heating/freezing which is used to predict the ore deposit type by Wilkinson (2000), classification diagram

| Sample | Type | Tmice (℃) | Th (℃) | Salinity (wt.%) | Density (g/m$^3$) |
|---|---|---|---|---|---|
| KB3-1 | Brt | − 6.2 | 280.1 | 9.47 | 0.841 |
| KB3-2 | Brt | − 6.2 | 276.5 | 2.41 | 0.841 |
| KB5 | Cal | − 11.6 | 231.3 | 15.5 | 0.954 |
| KB5 | Cal | − 11.5 | 240.4 | 15.4 | 0.944 |
| KB5 | Cal | − 11.7 | 270.1 | 15.7 | 0.913 |
| KB5 | Cal | − 11.8 | 235.4 | 15.8 | 0.952 |
| KB5 | Cal | − 11.5 | 239.2 | 15.5 | 0.945 |
| KB6C | Qtz | − 1.4 | 264 | 2.40 | 0.794 |
| KB6C | Qtz | − 4.5 | 228.1 | 7.17 | 0.909 |
| KB12-2 | Sl | − 10.4 | 219.5 | 14.4 | 0.957 |
| KB12-2a | Sl | − 11.5 | 228.4 | 15.5 | 0.956 |
| KB12-3 | Sl | − 11.5 | 197.5 | 15.5 | 0.987 |
| ML10 | Cal | − 14.2 | 249.8 | 18.0 | 0.955 |
| ML10 | Brt | − 11.2 | 209 | 15.2 | 0.974 |
| MLG2-4 | Sl | − 7.8 | 195.4 | 11.5 | 0.958 |
| MLG2-4 | Sl | − 9.7 | 191.5 | 13.6 | 0.979 |
| MLG2-4 | Brt | − 6.1 | 251.4 | 9.34 | 0.878 |
| ML-G3-1a | Sl | − 3.6 | 243.4 | 5.86 | 0.857 |
| ML-G3-1a | Sl | − 3.6 | 237.5 | 5.86 | 0.865 |
| ML-G3-1a | Sl | − 3.6 | 250.1 | 5.86 | 0.848 |
| ML-G3-1b | Brt | − 9.1 | 208 | 12.9 | 0.957 |
| MLG4-1 | Sl | − 9.4 | 232.5 | 13.3 | 0.934 |
| MLG4-1 | Sl | − 8.5 | 211.5 | 12.3 | 0.948 |
| MLG4-1 | Sl | − 4.5 | 210.5 | 7.17 | 0.909 |
| MLG4-2 | Sl | − 7.3 | 219.5 | 10.9 | 0.928 |
| MLG4-2 | Sl | − 10.4 | 215.4 | 14.4 | 0.961 |
| MLG4-2 | Sl | − 11.5 | 215.4 | 15.5 | 0.970 |
| MLG4-3 | Qtz | − 5.1 | 204 | 8.00 | 0.922 |

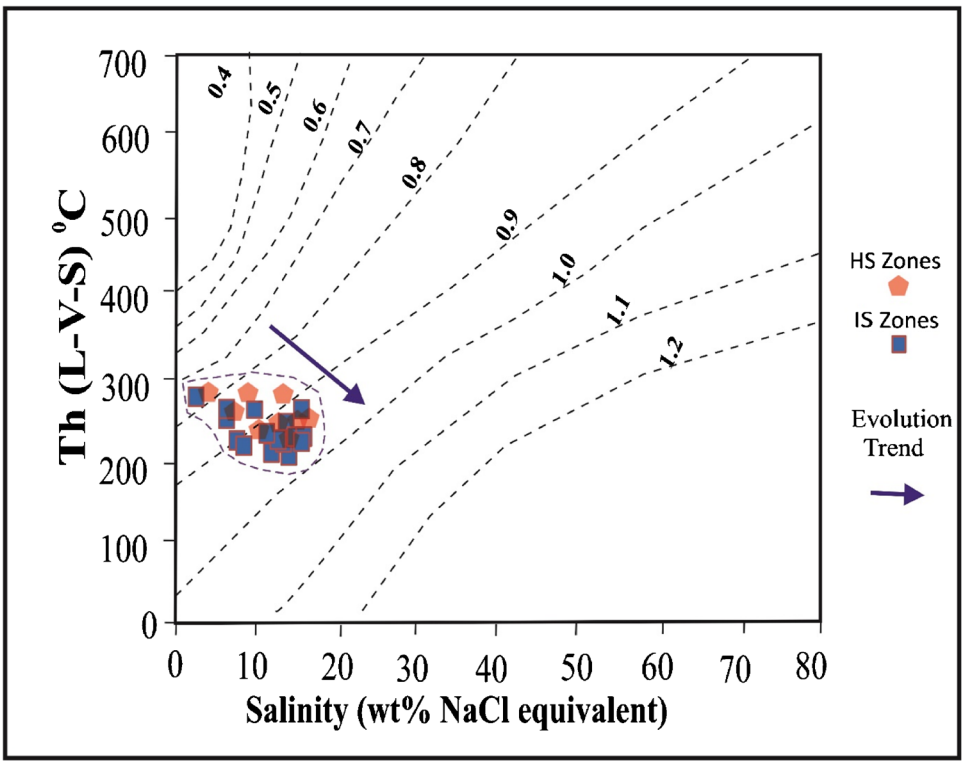


**Fig. 11** Fluid inclusion data on homogenization temperature and salinity diagram illustrating typical density ranges (g/cm.$^3$) for fluid inclusions (Brown 1989). HS, high sulphidation; IS, intermediate sulphidation

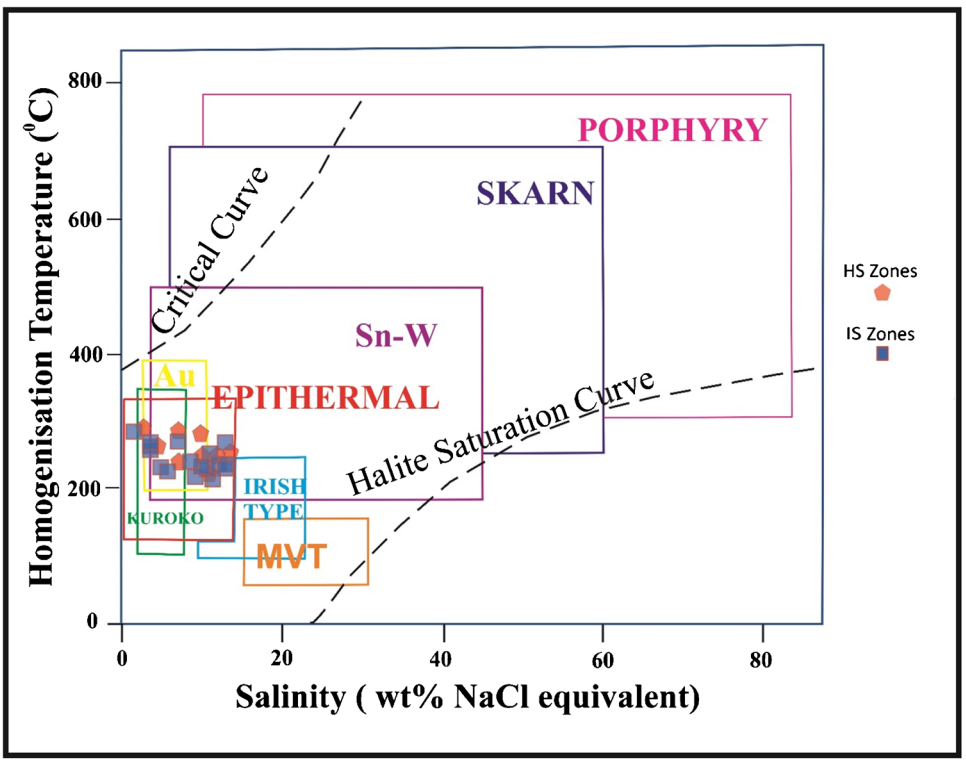


**Fig. 12** Homogenization (Th)–salinity diagram showing different areas for the fluid inclusion of various deposit types. Note that fields should not be considered definitive and compositions exist outside the ranges shown (Wilkinson 2001). HS, high sulphidation; IS, intermediate sulphidation

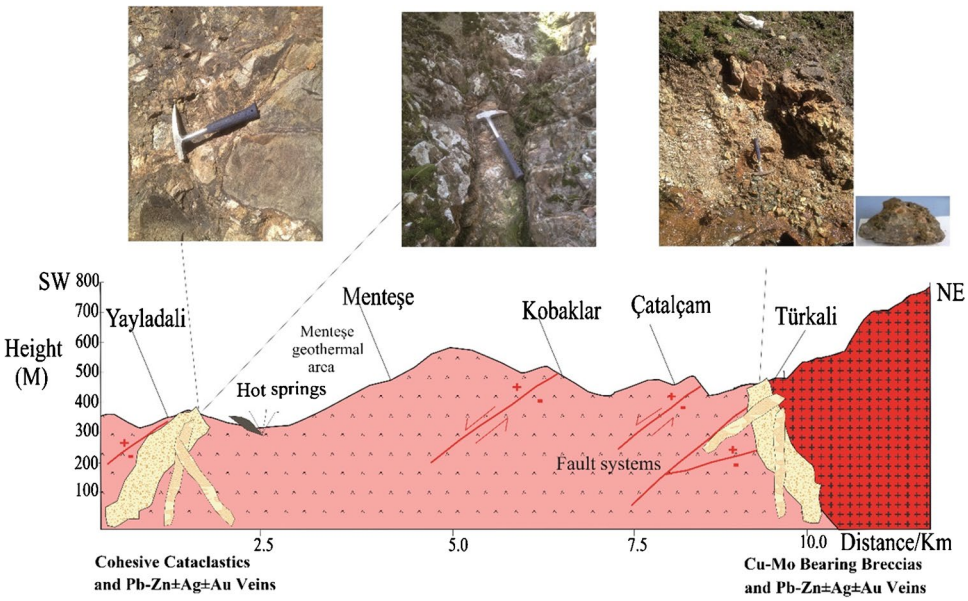


**Fig. 13** Simplified ore genesis model of the Northwest Soma (Manisa-Western Anatolia)

## Conclusion

The present study was carried out to determine the subtypes of mineralizations using ore mineralogy, alteration indexes (AI-CCPI), and fluid inclusions to understand fluid characteristics and traces of deposits. We revealed the following conclusions based on the integrated geochemistry, petrography, and fluid inclusion data obtained from the Soma Region (Manisa, NW Anatolia), which is characterized by numerous polymetallic, porphyry, and epithermal economic orebodies.

(1) Data from ore petrography, alteration indexes, and fluid inclusion studies are instrumental in characterizing fluids in vein-type mineralization and how they are associated with their original magma.
(2) The precipitation of Pb–Zn ± Au ± Ag in open-space fractures and vein/veinlets at the Yayladalı (Soma) region yields homogenization temperatures ranging between 192 and 280 ℃ with high salinity. The fluid inclusion data noticeably suggest the existence of both porphyry and hydrothermal-type mineralizations within the ore-forming system which was effective on the post-collisional intrusive and extrusive rocks in the region.
(3) In the Yayladalı region, the mineralization represents regions of high MgO and Low $Na_2O$ and gain or loss of $K_2O$. The mineralogy box plot reveals that alteration zones around Pb–Zn veins are either chlorite-quartz-carbonate or sericite-quartz-carbonate, with more chlorite-quartz-carbonate observed in the study area. For mineral exploration, the combination of AI and CCPI and mass change in MgO may give a better vector for mineralization.
(4) Polymetallic Pb–Zn ± Au ± Ag mineralization specifies an intermediate vein-type epithermal deposit similar to mineralizations in the region with temperature from 192 to 280 ℃ and salinity 2 to 17 wt.% NaCl equivalents which deposited more Pb and Zn than Au and Ag in open-space fractures and veins. Besides, the Cu and Mo presumably originated from the Turkali pluton, classified predominantly as granite-granodiorite in composition.
(5) Deep-seated high-sulphidation acidic fluid might have migrated to the lithocap and moved through wall rock water reaction by neutralizing and reducing this fluid to form intermediate sulphidation veins (Fig. 13). As shown by fluid inclusion data, the intermediate sulphidation fluids with high salinity favor the precipitation of base metal Zn-Cu-Pb-Ag than precious metal Au. A more complete understanding of the ore-forming system in the region must be examined through interdisciplinary detailed studies.

**Acknowledgements** This study is a part of the M.Sc. thesis of Muhammed Kabiru. It is financially supported by the Scientific Research Office of Istanbul Technical University (ITUBAP Project Code 39797). We would like to express our gratitude to the reviewers for helpful criticism and suggestions that improved the manuscript.

**Data availability** Some or all data that support the findings of this study are available from the corresponding author upon reasonable request.

## Declarations

**Conflict of interest** The authors declare that they have no competing interests.

## References


Akal C (2013) Coeval Shoshonitic-ultrapotassic dyke emplacements within the Kestanbol pluton, Ezine-Biga peninsula (NW Anatolia). Turk J Earth Sci 22(2):220–238. https://doi.org/10.3906/sag-1212-62

Akiska S, Demirela G, Sayili Sİ (2013) Geology, mineralogy and the Pb, S isotope study of the Kalkım Pb-Zn±Cu deposits, Biga Peninsula. NW Turkey J Geosci-Czech 58(4):379–396. https://doi.org/10.3190/jgeosci.154

Akiska S (2020) Crystallization conditions and compositional variations of silicate and sulfide minerals in the Pb-Zn skarn deposits, Biga Peninsula. NW Turkey Ore Geol Rev 118:103322. https://doi.org/10.1016/j.oregeorev.2020.103322

Aldanmaz E (2006) Mineral-chemical constraints on the Miocene calc-alkaline and shoshonitic volcanic rocks of western Turkey: disequilibrium phenocryst assemblages as indicators of magmastorage and mixing conditions. Turk J Earth Sci, 15(1), 47–73. https://journals.tubitak.gov.tr/earth/issues/yer-06-15-1/yer-15-1-3-0509-1.pdf

Altunkaynak Ş, Yilmaz Y (1999) The Kozak Pluton and its emplacement. Geol J 34(3):257–274. https://doi.org/10.1002/(SICI)1099-1034(199907/09)34:3<257::AID-GJ826>3.0.CO;2-Q

Altunkaynak Ş, Genç ŞC (2008) Petrogenesis and time-progressive evolution of the Cenozoic continental volcanism in the Biga Peninsula, NW Anatolia (Turkey). Lithos 102(1–2):316–340. https://doi.org/10.1016/j.lithos.2007.06.003

BAS ML, Maitre RL, Streckeisen A, Zanettin B, IUGS Subcommission on the Systematics of Igneous Rocks (1986) A chemical classification of volcanic rocks based on the total alkali-silica diagram. J Petrol 27(3):745–750

Bingöl E, Akyürek B, Korkmazer B (1973) Geology of the Biga Peninsula and some characteristics of the Karakaya Formation. In Proceedings of the 50th Anniversary of Turkish Republic Earth Science Congress Ankara pp 70–7

Black KN, Catlos EJ, Oyman T, Demirbilek M (2012) Relationships between subduction and extension in the Aegean region: evidence from granite plutons of the Biga Peninsula, NW Turkey. Geophys Res Abstr 14:EGU2012-814

Bodnar RJ (1993) Revised equation and table for determining the freezing point depression of H2O-NaCl solutions. Geochim Cosmochim Acta 57(3):683–684

Bodnar RJ, Lecumberri-Sanchez P, Moncada D, Steele-MacInnis M (2014) Fluid inclusions in hydrothermal ore deposits, treatise on geochemistry: second edition. https://doi.org/10.1016/B978-0-08-095975-7.01105-0.

Boynton WV (1984) Cosmochemistry of the rare earth elements: meteorite studies. Dev Geochem 2:63–114. https://doi.org/10.1016/B978-0-444-42148-7.50008-3

Bozkaya G, Gökce A (2009) Lead and sulfur isotope studies of the Koru (Çanakkale, Turkey) lead-zinc deposits. Turk J Earth Sci, 18(1), 127–137. https://journals.tubitak.gov.tr/earth/issues/yer-09-18-1/yer-18-1-6-0806-5.pdf

Bozkaya G, Banks D, Ozbas F, Wallington J (2014) Fluid processes in the Tesbihdere base-metal-Au deposit: implications for epithermal mineralization in the Biga Peninsula, NW Turkey. Open Geosci 6(2):148–169. https://doi.org/10.2478/s13533-012-0169-9

Bozkaya G, Banks DA (2016) Sulfur isotope geochemistry and mineralogy of Balcilar vein type barite-sulphide mineralization, Biga Peninsula, NW Turkey. Pamukkale Un J of Eng Sci 22(3):200–205. https://doi.org/10.5505/pajes.2014.87699

Bozkaya G, Bozkaya Ö, Banks DA, Gökçe A (2020) PTX constraints on the Koru epithermal base-metal (±Au) deposit, Biga Peninsula, NW Turkey. Ore Geol Rev 119:103349. https://doi.org/10.1016/j.oregeorev.2020.103349

Bozkaya Ö, Bozkaya G, Uysal IT, Banks DA (2016) Illite occurrences related to volcanic-hosted hydrothermal mineralization in the Biga Peninsula, NW Turkey: implications for the age and origin of fluids. Ore Geol Rev 76:35–51. https://doi.org/10.1016/j.oregeorev.2016.01.001

Brown PE (1989) FLINCOR; a microcomputer program for the reduction and investigation of fluid-inclusion data. Amer Miner 74(11–12):1390–1393

Cicek M, Oyman T (2016) Origin and evolution of hydrothermal fluids in epithermal Pb-Zn-Cu±Au±Ag deposits at Koru and Tesbihdere mining districts, Çanakkale, Biga Peninsula, NW Turkey. Ore Geol Rev 78:176–195. https://doi.org/10.1016/j.oregeorev.2016.03.020

Dilek Y, Altunkaynak Ş (2009) Geochemical and temporal evolution of Cenozoic magmatism in western Turkey: mantle response to collision, slab break-off, and lithospheric tearing in an orogenic belt. Geological Society, London, Special Publications. 311 (1): 213–233. https://sp.lyellcollection.org/content/311/1/213.full

Ersoy EY, Helvacı C, Uysal I, Karaoğlu Ö, Palmer MR, Dindi F (2012) Petrogenesis of the Miocene volcanism along the İzmir-Balıkesir Transfer Zone in western Anatolia, Turkey: implications for origin and evolution of potassic volcanism in post-collisional areas. J Volcanol Geotherm Res 241:21–38. https://doi.org/10.1016/j.jvolgeores.2012.05.022

Ersoy EY, Palmer MR, Genç ŞC, Prelević D, Akal C, Uysal I (2017) Chemo-probe into the mantle origin of the NW Anatolia Eocene to Miocene volcanic rocks: implications for the role of, crustal accretion, subduction, slab roll-back and slab break-off processes in genesis of post-collisional magmatism. Lithos 288:55–71. https://doi.org/10.1016/j.lithos.2017.07.006

Franklin JM, Gubins AG (1997) Lithogeochemical and mineralogical methods for base metal and gold exploration. Proc Explor 97:191–208

Goldstein RH, Samson I, Anderson A, Marshall D (2003) Petrographic analysis of fluid inclusions. Fluid Inclusions: Analysis and Interpretation 32:9–53

Gökce A, Bozkaya G (2007) Lead and sulfur isotopic studies of the barite–galena deposits in the Karalar area (Gazipaşa–Antalya), Southern Turkey. J Asian Earth Sci 30(1):53–62. https://doi.org/10.1016/j.jseaes.2006.07.007

Hedenquist JW, Arribas A, Gonzalez-Urien E (2000) Exploration for epithermal gold deposits. Rev Econ Geol 13(2):45–77. https://doi.org/10.5382/Rev.13.07

Kabiru M (2017) Genesis of polymetallic (Pb-Zn-Cu±Ag±Au) mineralization at Yayladali and its environs (Manisa), Turkey, M.Sc. Thesis, Faculty of Mines, Istanbul Technical University, Istanbul, Turkey

Kabiru M, Kocaturk H, Yıldırım D, Kumral M, Unluer AT, Budakoglu M (2018) Characterization of Turkali Pluton & Yuntdag Volcanics related Ore Genesis (Manisa-Turkey). Magmatism of the Earth and Related Strategic Metal Deposits 1:124–127

Kasapçı C, Öztürk H, Hanilçi N, Aysal N (2008) Formation of the Arapuçan Dere (Yenice–Çanakkale) Pb-Zn-Cu deposit in the light of the geological and fluid inclusion findings. In Türkiye Kurşun-Çinko Yataklarının Jeolojisi, Madenciliği Ve Mevcut Sorunları Sempozyumu Bildiriler Kitabı (pp. 100–118).

Ishikawa Y, Sawaguchi T, Iwaya S, Horiuchi (1976) Delineation of prospecting targets for Kuroko deposits based on. Mining Geology

26(136):105–117. https://doi.org/10.11456/shigenchishitsu1951.26.105
Klyukin YI, Steele-MacInnis M, Lecumberri-Sanchez P, Bodnar RJ (2019) Fluid inclusion phase ratios, compositions and densities from ambient temperature to homogenization, based on PVTX properties of H2ONaCl. Earth-Sci Rev 198:102924. https://doi.org/10.1016/j.earscirev.2019.102924
Kuşcu İ, Tosdal RM, Gençalioğlu-Kuşcu G. (2019). Porphyry-Cu deposits of Turkey. Mineral Resources of Turkey, 337–425. https://link.springer.com/chapter/10.1007/978-3-030-02950-0_8
Large RR, Allen RL, Blake MD, Herrmann W (2001a) Hydrothermal alteration and volatile element halos for the Rosebery K lens volcanic-hosted massive sulfide deposit, western Tasmania. Econ Geol 96(5):1055–1072. https://doi.org/10.2113/gsecongeo.96.5.1055
Large RR, Gemmell JB, Paulick H, Huston DL (2001b) The alteration box plot: a simple approach to understanding the relationship between alteration mineralogy and lithogeochemistry associated with volcanic-hosted massive sulfide deposits. Econ Geol 96(5):957–971. https://doi.org/10.2113/gsecongeo.96.5.957
Leroux GM (2016) Stratigraphic and petrographic characterization of HS epithermal Au-Ag mineralization at the TV Tower district, Biga Peninsula, NW Turkey. Doctoral dissertation, University of British Columbia. https://doi.org/10.14288/1.0300312
Okay AI, Siyako M, Bürkan KA (1991) Geology and tectonic evolution of the Biga Peninsula, northwest Turkey. Bull Tech Uni Istanbul 44(1–2):191–256
Okay A, Altiner D (2004) Uppermost Triassic limestone in the Karakaya Complex-stratigraphic and tectonic significance. Turk J Earth Sci, 13(2), 187–199. https://journals.tubitak.gov.tr/earth/issues/yer-04-13-2/yer-13-2-5-0406-4.pdf
Okay A, Göncüoğlu MC (2004) The Karakaya Complex: a review of data and concepts. Turkish J Earth Sci, 13(2), 75–95. https://journals.tubitak.gov.tr/earth/issues/yer-04-13-2/yer-13-2-1-0406-3.pdf
Özdamar Ş, Roden MF, Zou H, Billor MZ, Hames W, GeorgievS, Dunkl I (2021) Petrogenesis of Oligocene plutonic rocks in western Anatolia (NW Turkey): insights from mineral and rock chemistry, Sr-Nd isotopes, and U-Pb, Ar-Ar and (U-Th)/He geochronology. Chem Erde, 125747https://doi.org/10.1016/j.chemer.2021.125747
Özpınar Y, Kılıç M, Avşar M, Sarı R, Küçükefe Ş, Agnerian H, Doygun Z, Yenigün K (2012) A new assessment of the Kısacık gold mineralization (Ayvacik-Çanakkale; NW Anatolia). Roman J Earth Sci 86(2):111–116
Pirajno F (1995) Volcanic-hosted epithermal systems in northwest Turkey. South African J of Geol, 98(1), 13–24. https://hdl.handle.net/10520/EJC-928e97d24
Roedder E (1984) Fluid inclusions. Reviews in Mineralogy. Mineral Soc of Amer 12:644
Sánchez MG, McClay K, King A (2016) Cenozic crustal extension and its relationship to porphyry Cu-Au and epithermal Au mineralization in the Biga Peninsula, NW Turkey. Soc Econ Geol Spec Publ 19:113–156. https://doi.org/10.5382/SP.19.05
Sari R, Kucukefe S, Bozkaya G, Bozkaya O, Bademler F, Aral ZD, Bayrakcioglu ED, Donmez C, Ozkumuş S (2021) Geological, Mineralogical-petrographical and fluid-inclusion characteristics of the Catalcam (Soma-Manisa) Au-Pb-Zn-Cu mineralization. Bullet of MTA, 165, (In Press) https://doi.org/10.19111/bulletinofmre.930094
Sayit K, Göncüoglu MC (2009) Geochemical characteristics of the basic volcanic rocks within the Karakaya Complex: a review. Yerbilimleri 30:181–191
Seghedi I, Helvacı C, Pécskay Z (2015) Composite volcanoes in the south-eastern part of İzmir-Balıkesir transfer zone, Western Anatolia, Turkey. J of Volcan and Geotherm Res 291:72–85. https://doi.org/10.1016/j.jvolgeores.2014.12.019
Smith MT, Lepore WA, IncekaraoğluT SP, BoranH RK (2014) Küçükdağ: a new, high sulfidation epithermal Au-Ag-Cu deposit at the Tv tower property in western Turkey. Econ Geol 109(6):1501–1511. https://doi.org/10.2113/econgeo.109.6.1501
Sun SS, McDonough WF (1989) Chemical and isotopic systematics of oceanic basalts: implications for mantle composition and processes. Geol Soc, London, Special Publications 42(1):313–345. https://doi.org/10.1144/GSL.SP.1989.042.01.19
Steele-MacInnis M, Lecumberri-Sanchez P, Bodnar RJ (2012) HOKIEFLINCS_H2O-NACL: a Microsoft Excel spreadsheet for interpreting microthermometric data from fluid inclusions based on the PVTX properties of H2O-NaCl. Comput and Geosci 49:334–337
Tekeli O (1981) Subduction complex of pre-Jurassic age, northern Anatolia. Turkey. Geology 9(2):68–72
Van den Kerkhof AM, Hein UF (2001) Fluid inclusion petrography. Lithos 55(1–4):27–47. https://doi.org/10.1016/S0024-4937(00)00037-2
Wilkinson JJ (2001) Fluid inclusions in hydrothermal ore deposits. Lithos 55(1–4):229–272. https://doi.org/10.1016/S0024-4937(00)00047-5
Yigit O (2006) Gold in Turkey—a missing link in Tethyan metallogeny. Ore Geol Rev 28(2):147–179. https://doi.org/10.1016/j.oregeorev.2005.04.003
Yigit O. (2007). Recent discoveries and exploration trends in Turkey. Digging Deeper, Vols 1 and 2: Digging Deeper. Irish Assoc Econ Geol, Dublin 4
Yigit O (2009) Mineral deposits of Turkey in relation to Tethyan metallogeny: implications for future mineral exploration. Econ Geol 104(1):19–51. https://doi.org/10.2113/gsecongeo.104.1.19
Yigit O (2012) A prospective sector in the Tethyan Metallogenic Belt: geology and geochronology of mineral deposits in the Biga Peninsula, NW Turkey. Ore Geol Rev 46:118–148. https://doi.org/10.1016/j.oregeorev.2011.09.015
Yilmaz Y (1989) An approach to the origin of young volcanic rocks of western Turkey. Tectonic Evolution of the Tethyan Region, 159-189https://doi.org/10.1007/978-94-009-2253-2_10
Yilmaz H, Oyman T, Arehart GB, Colakoglu AR, Billor Z (2007) Low-sulfidation type Au–Ag mineralization at Bergama, Izmir, Turkey. Ore Geol Rev 32(1–2):81–124. https://doi.org/10.1016/j.oregeorev.2006.10.007
Yilmaz H, Oyman T, Sonmez FN, Arehart GB, Billor Z (2010) Intermediate sulfidation epithermal gold-base metal deposits in Tertiary subaerial volcanic rocks, Sahinli/Tespih Dere (Lapseki/Western Turkey). Ore Geol Rev 37(3–4):236–258. https://doi.org/10.1016/j.oregeorev.2010.04.001
Yilmaz H, Sönmez FN, Erhan A, Şener AK, Tufan ST (2013) Low-sulfidation epithermal Au-Ag mineralization in the Sındırgı District, Balıkesir Province, Turkey. Turk J Earth Sci 22(4):485–522. https://doi.org/10.3906/tar-1206-8